Title:

Reduced Thalamic Excitation to Motor Cortical Pyramidal Tract Neurons in Parkinsonism

Liqiang Chen[1,2], Samuel Daniels[1], Rachel Dvorak[1], and Hong-Yuan Chu[1,2*]

[1]Department of Neurodegenerative Science, Van Andel Institute, Grand Rapids, MI 49503 USA

[2]Aligning Science Across Parkinson's (ASAP) Collaborative Research Network, Chevy Chase, MD 20815

[*]Correspondence: hongyuan.chu@vai.org

Address: 333 Bostwick Ave NE, Grand Rapids, MI 49503

Phone: 616-234-5847

Competing interests: The authors declare no competing interests.

Acknowledgement: The authors thank the Van Andel Institute optical imaging core for the advanced confocal microscope, and Van Andel Institute vivarium for animal husbandry. The authors thank all members of the Chu lab and Dr. Martha L Escobar Galvis at Van Andel Institute for thoughtful discussions and scientific editing. Funding: The research in Dr. Chu's lab is supported by the National Institute of Neurological Disorders and Stroke (grant#: R01NS121371 for H.Y.C.) and Aligning Science Across

Parkinson's (ASAP-020572 for H.Y.C.) through the Michael J Fox Foundation for Parkinson's Research (MJFF). For the purpose of open access, the authors have applied a CC BY public copyright license to all Author Accepted Manuscripts arising from this submission. Authors' contribution: investigation, formal analysis (LC/SD/RD/HYC); conceptualization, funding acquisition, project administration, resources, supervision, visualization, writing – original draft (HYC); Writing – review& editing (LC/SD/HYC).

Abstract

Degeneration of midbrain dopaminergic (DA) neurons alters the connectivity and functionality of the basal ganglia-thalamocortical circuits in Parkinson's disease (PD). Particularly, the aberrant outputs of the primary motor cortex (M1) contribute to parkinsonian motor deficits. However, cortical adaptations at cellular and synaptic levels in parkinsonism remain poorly understood. Using multidisciplinary approaches, we found that DA degeneration induces cell-subtype- and input-specific reduction of thalamic excitation to M1 pyramidal tract (PT) neurons. At molecular level, we identified that NMDA receptors play a key role in mediating the reduced thalamocortical excitation to PT neurons. At circuit level, we showed that the reduced thalamocortical transmission in parkinsonian mice can be rescued by chemogenetically suppressing basal ganglia outputs. Together, our data suggest that cell subtype- and synapse-specific adaptations in M1 contribute to altered cortical outputs in parkinsonism and are important aspects of PD pathophysiology.

Teaser

Neuroplasticity in the cerebral cortex contributes to parkinsonian pathophysiology

Key words

6-hydroxydopamine, basal ganglia, chemogenetics, dopamine, electrophysiology, motor cortex, neuroplasticity, NMDA receptor, optogenetics, Parkinson's disease, thalamus

Introduction

Degeneration of dopaminergic (DA) neurons in the substantia nigra *pars* compacta (SNc) alters the magnitude and temporal pattern of basal ganglia (BG) outputs to downstream motor regions and has been causally linked to the motor deficits in Parkinson's disease (PD) (*1*–*3*). The substantia nigra *pars* reticulata (SNr) is the major BG output structure in rodents and sends GABAergic projections to the motor region of the thalamus (mTh), including the ventromedial (VM) and ventral anterior-lateral (VAL) thalamus (*4*–*7*). The mTh transmits motor selection and execution information to cortical regions for proper motor control (*8*–*11*). Thus, in PD the thalamocortical network occupies a critical position in mediating motor symptoms, particularly the disruption of voluntary movements (*12*–*16*).

The primary motor cortex (M1) plays a key role in sensorimotor integration and proper control of motor behaviors (*17*–*19*). Its involvement into pathophysiology of parkinsonian motor symptoms was proposed by the rate model of BG-thalamocortical network and further supported by recent experimental evidence (*1*, *12*–*14*, *20*–*22*). However, considering the heterogeneity and complexity of cortical cell subtypes and their associated synaptic connections, our understanding of M1 circuit dysfunction in PD remains limited. For example, how do basal ganglia dysfunction and/or DA neurodegeneration affect the structural and functional connectivity of M1 circuits? How does M1 circuit dysfunction at macroscopic and microscopic levels contribute to PD symptoms? Answers to these questions are needed to advance our understanding of circuit pathophysiology in PD.

Research suggests that M1 circuits exhibit specific alterations in parkinsonism. Loss of SNc DA neurons alters neuronal firing and synaptic connectivity of M1 pyramidal

neurons (*12*, *23*–*25*). Particularly, DA depletion selectively affects the activity of pyramidal tract (PT) neurons, but not the intratalencephalic (IT) neurons, in the layer V of M1 (*12*, *14*, *21*, *26*). These structural and functional changes perhaps contribute to the rewired cortical motor representation and impaired forelimb function in parkinsonian state (*27*–*29*). Building on these observations, we hypothesized that degeneration of SNc DA neurons induces cell-subtype- and input-specific adaptations in M1 circuits. Our results largely agree with our predictions and provide a detailed description that contributes to mechanistic understanding of M1 circuitry adaptations in parkinsonism.

Results

Mice received either 6-hydroxydopamine (6-OHDA) injection into the medial forebrain bundle (MFB) to induce the degeneration of nigrostriatal pathway and SNc DA neurons ("6-OHDA mice" herein), or vehicle injection into the MFB as controls ("controls" herein). Physiological and anatomical studies were conducted between 3–5 weeks post-injections. To interrogate synaptic properties of thalamocortical inputs to projection-defined subtypes of cortical pyramidal neurons in controls and 6-OHDA mice, we stereotaxically injected: (1) AAV9-hSyn-ChR2(H134R)-eYFP into the mTh, centering at the VM thalamus (**Figure. 1A, B**); (2) Retrobeads into the ipsilateral pontine nuclei and contralateral striatum to label PT and IT neurons, respectively (**Figure. 1A**). Three weeks post-injection, intense eYFP labeled fibers could be observed, particularly in layers I and V of M1 (**Figure 1B**) (*8*, *30*). Synaptic strength of thalamic inputs to retrogradely labeled neurons was measured as the amplitude of optogenetically-evoked excitatory postsynaptic currents (oEPSCs) at a holding potential of –80 mV, which were mainly mediated by AMPA and NMDA receptors (Rs) (**Figure S1**).

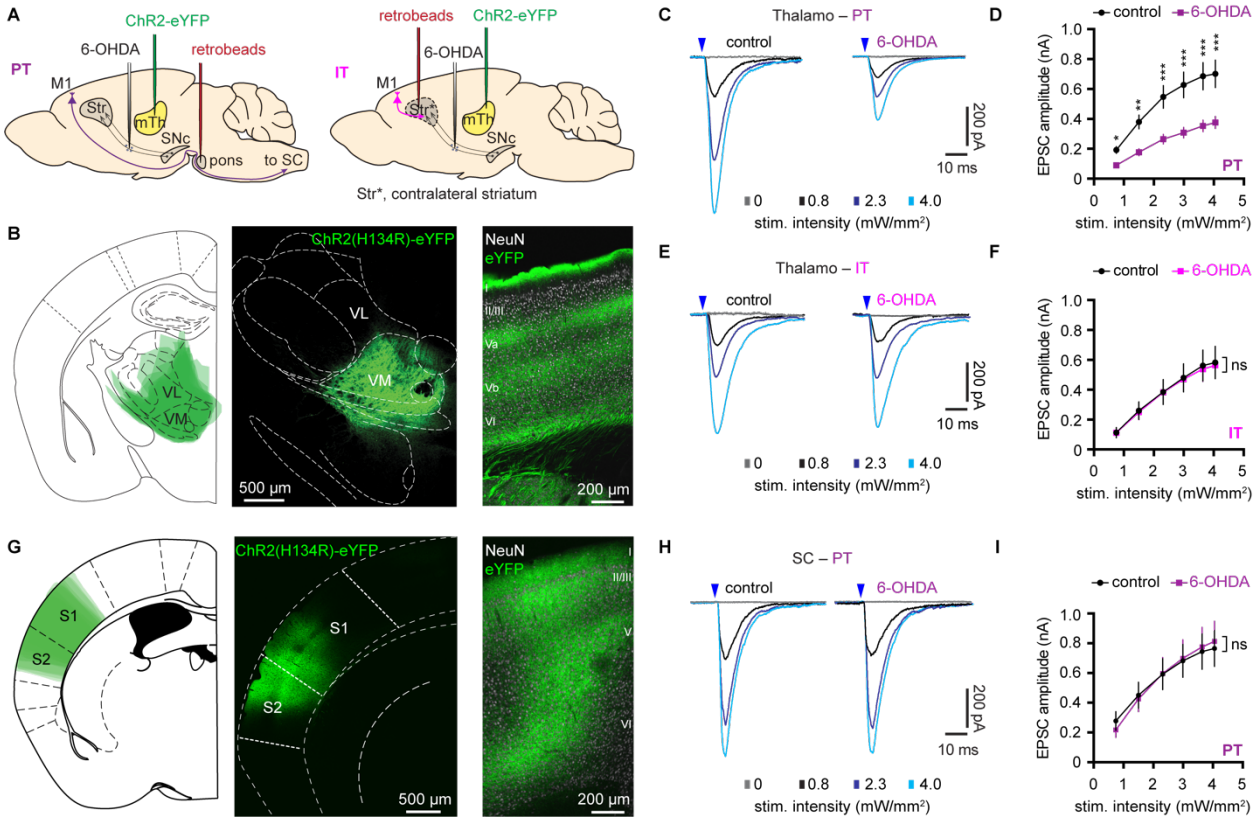

Figure 1. SNc DA degeneration induces cell-subtype- and input-specific alterations in M1. A) Schematic of overall strategies to retrogradely label M1 pyramidal neurons based on their projections and to selectively activate thalamocortical transmission arising from the motor thalamus (mTh) of both controls and 6-OHDA mice using AAV-mediated optogenetics. **B**) AAV-infected areas across mice were overlaid to show the averaged AAV injection sites in the motor thalamus (left), as well as representative confocal images showing an example of viral injection site in the motor thalamus (middle) and eYFP-expressing thalamic axon terminals in the M1 of a mouse (right). eYFP-labeled terminals concentrate in the layers I and V and are consistent with the overall pattern of motor thalamic innervation of M1 in rodents. **C-D**) Representative traces of optogenetically-evoked EPSCs across different stimulation intensities in PT neurons from controls and 6-OHDA mice (C) and the summarized results (D). $P < 0.0001$ between groups, mixed effects model followed by Sidak's tests. *, $p < 0.05$, **, $p < 0.01$, ***, $p < 0.001$ relative to controls. Control = 62 cells/7 mice; 6-OHDA = 73 cells/8 mice. **E-F**) Representative traces of optogenetically-evoked EPSCs across different stimulation intensities in IT neurons from both controls and 6-OHDA mice (E) and the summarized results (F). ns, not significant between groups, mixed effects model. 26 cells/3 mice for each group. **G**) AAV-infected cortical regions were overlaid to show the averaged AAV infection region across animals (left) and representative confocal images showing AAV9-ChR2(H134R)-eYFP infusion site in the sensory cortical areas (middle), and eYFP-expressing cortical axon terminals in the M1 (right). **H-I**) Representative traces of optogenetically-evoked EPSCs arising from the SC across different stimulation intensities in M1 PT neurons from both controls and 6-OHDA mice (H) and the summarized results (I). Control = 20 cells/3 mice, 6-OHDA = 26 cells/3 mice. Mixed effects model, ns, not significant between groups. Arrowheads in *C, E, H* indicate the timing of the optical stimulation.

SNc DA degeneration induces cell-subtype- and input-specific alterations in M1

Whole-cell voltage-clamp recordings were conducted in the presence of TTX (1 μM) and 4-AP (100 μM) to prevent the engagement of polysynaptic responses and facilitate optogenetically evoked glutamate release from thalamic axon terminals (*8*, *31*). The amplitude of thalamic oEPSCs in PT neurons (thalamo-PT) from the ipsilateral hemisphere with lesion was greatly reduced in 6-OHDA mice relative to those from controls across a range of stimulation intensities (**Figure 1C, D**). However, the amplitude of thalamo-PT oEPSCs from the DA-intact contralateral hemisphere was unaltered (**Figure S2**), suggesting that the reported compensation in the contralateral hemisphere of hemiparkinsonism may not occur at the thalamocortical connections (*32*). Thus, studies in the rest of this work will mainly focus on synaptic adaptations in the ipsilateral hemisphere. Moreover, the amplitude of oEPSCs in the IT neurons (thalamo-IT) was similar between 6-OHDA mice and controls (**Figure 1E, F**). These data suggest that chronic SNc DA degeneration selectively decreases synaptic strength of the motor thalamic excitation to M1 PT neurons in the hemisphere with lesion.

Multiple long-range cortical and thalamic excitatory inputs converge on M1 pyramidal neurons (*8*). Thus, we examined whether SNc DA degeneration also affects other excitatory inputs to PT neurons. We injected AAV-hSyn-ChR2(H134R)-eYFP into the sensory cortical (SC) regions (**Figure 1G**) and retrobeads into the pons to retrogradely label PT neurons. The amplitude of oEPSCs from SC to PT neurons (SC-PT) was not altered between 6-OHDA mice and controls (**Figure 1H, I**). These data suggest that DA degeneration induces input-specific changes to M1 PT neurons. Altogether, chronic DA degeneration triggers cell-subtype- and input-specific adaptions in M1 local circuits.

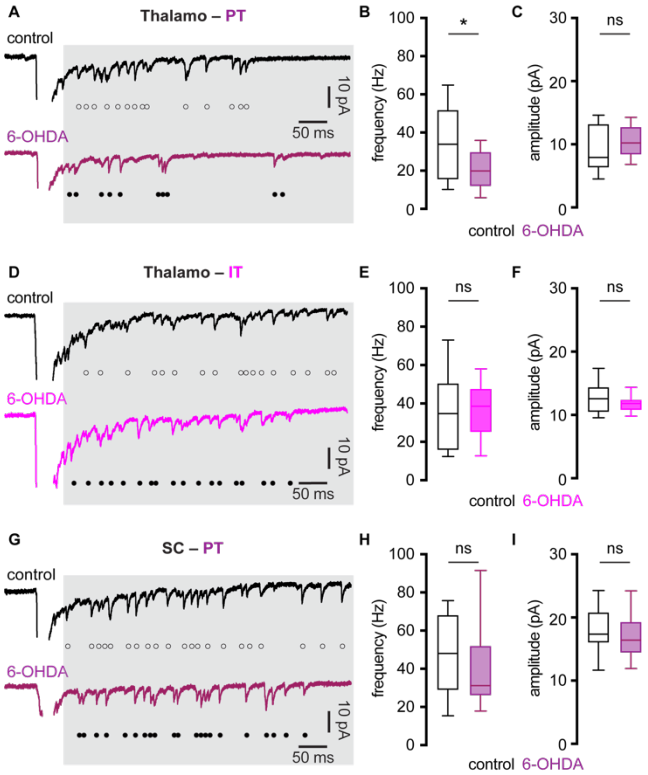

Figure 2. SNc DA degeneration decreases the number of functional thalamic inputs to PT neurons. A) Representative traces showing optogenetically-evoked, Sr^{2+}-induced asynchronous thalamocortical EPSCs of PT neurons from controls and 6-OHDA mice. Open and filled circle indicate individual events of asynchronous EPSCs. **B-C**) Box plots showing a reduced frequency (B, controls = 34 [15.5–52] Hz, n = 20 neurons/3 mice; 6-OHDA = 20 [12–30] Hz, n = 20 neurons/4 mice; p = 0.02, Mann-Whitney U test (MWU)) and unaltered amplitude (C, controls = 7.95 [6.3–13.2] pA, n = 20 neurons/3 mice; 6-OHDA = 10.2 [8.4–12.8] pA, n = 20 neurons/4 mice; p = 0.33, MWU) of Sr^{2+}-EPSCs at thalamo-PT synapses from 6-OHDA mice relative to controls. **D**) Representative traces showing optogenetically-evoked, Sr^{2+}-induced quantal EPSCs at thalamo-IT synapses from controls and 6-OHDA mice. Open and filled circle indicate individual events of asynchronous EPSCs. **E-F**) Box plots showing unaltered frequency (E, controls = 34.8 [15.7–50.5] Hz, n = 22 neurons/3 mice; 6-OHDA = 38.4 [24.9–47.6] Hz, n = 22 neurons/3 mice; p = 0.7, MWU) and amplitude (F, control = 12.6 [10.5–14.4] pA; 6-OHDA = 11.8 [10.8–12.4] pA; n = 22 neurons/3 mice; p = 0.34, MWU) of Sr^{2+}-EPSCs at thalamo-IT synapses between groups. **G**) Representative traces showing optogenetically-evoked, Sr^{2+}-induced quantal EPSCs at SC-PT synapses from controls and 6-OHDA mice. Open and filled circles indicate individual events of asynchronous EPSCs. **H-I**) Box plots showing unaltered frequency (H, controls = 48 [29–68] Hz, n = 20 neurons/3 mice; 6-OHDA = 31.2 [26–52] Hz, n = 19 neurons/3 mice; p = 0.6, MWU) and amplitude (I, control = 17 [16–20.8] pA, n = 20 neurons/3 mice; 6-OHDA = 16.5 [14.4–19.3] pA, n = 19 neurons/3 mice; p = 0.5, MWU) of Sr^{2+}-EPSCs at SC-PT synapses between groups. ns, not significant. All data are reported as median and interquartile range (in square brackets).

SNc DA degeneration decreases the number of functional thalamic inputs to PT neurons

DA degeneration did not alter the paired pulse ratio (PPR) at thalamo-PT, thalamo-IT or SC-PT synapses (**Figure S3**), suggesting that the selective reduction of thalamic excitation to PT neurons was not due to a lower initial release probability at thalamo-PT synapses. To understand presynaptic mechanisms underlying synaptic adaptations of M1 circuits following the loss of SNc DA neurons, we assessed the quantal properties of thalamic glutamatergic neurotransmission to PT and IT neurons (*30*, *33*, *34*). Replacing extracellular Ca^{2+} with Sr^{2+} (2 mM), we found a significant reduction of the frequency, but not the amplitude, of optogenetically-evoked asynchronous EPSCs (Sr^{2+}-EPSCs) at the thalamo-PT synapses from 6-OHDA mice relative to controls (**Figure 2A-C**). In contrast, neither the frequency nor the amplitude of Sr^{2+}-EPSCs at the thalamo-IT synapses was altered in 6-OHDA mice relative to controls (**Figure 2D-F**). Moreover, neither the frequency nor the amplitude of Sr^{2+}-EPSCs at SC–PT synapses was altered by DA depletion (**Figure 2G-I**). These data further support that SNc DA degeneration selectively decreases the connection strengthen of thalamic projection to PT neurons, at least partially due to fewer functional thalamo-PT connections.

SNc DA degeneration induces structural changes of thalamocortical synapses to PT neurons

To assess how loss of DA alters thalamocortical innervation of M1 PT neurons, brain sections from control and 6-OHDA mice were processed for immunohistochemical detection of vesicular glutamate transporter 2 (vGluT2), a marker of thalamic axon

boutons in M1. Stereological methods were used to quantify vGluT2-immunoreactive (vGluT2-ir) puncta in the layer V of M1. Consisted with findings from MPTP-treated non-human primates (*24*), the density of vGluT2-ir puncta in layer V was significantly decreased in slices from 6-OHDA mice relative to those from controls (**Figure 3A-C**). Thus, DA depletion likely induces a loss of presynaptic thalamic axon terminals in M1, though a potential decrease in vGluT2 expression cannot be excluded.

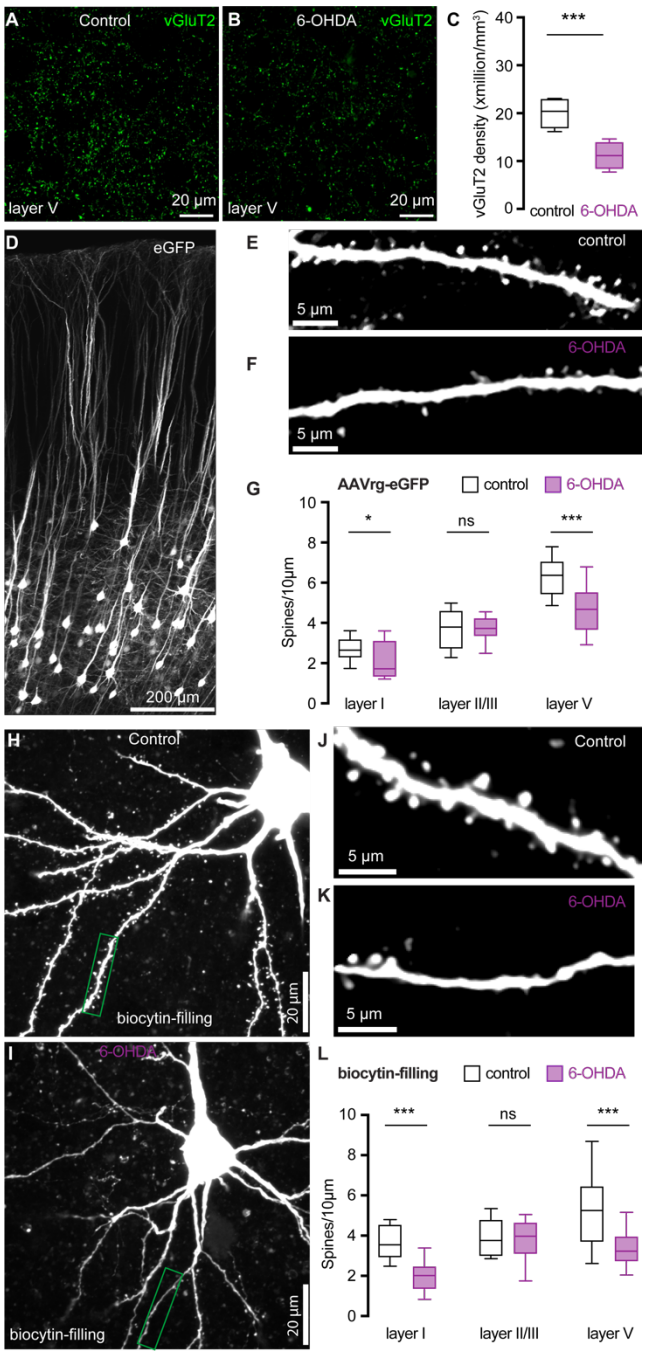

Figure 3. SNc DA degeneration alters the structure of thalamocortical synapses to PT neurons. A-C) Representative confocal images of vGluT2-immunoreactivity in the layer 5 of M1 from controls (A) and 6-OHDA mice (B), and the summarized results showing a reduced vGluT2 density in the layer V of M1 following the SNc DA degeneration (C, control = 20.4 [16.9–22.9] million puncta/mm^3, n = 20 slices/3 mice; 6-OHDA = 11.2 [8.5–13.9] million puncta/mm^3, n = 20 slices/3 mice; $p < 0.0001$, MWU). **D-F**) Representative confocal images of eGFP-labeled PT neurons in M1 (D) and segments of basal dendrites from controls (E) and 6-OHDA mice (F). **G**) Summarized results showing decreased spine densities of layer V basal dendrites (control = 6.4 [5.4–7.1] per 10 µm, n = 53 segments/3 mice; 6-OHDA = 4.7 [3.6–5.5] per 10 µm, n = 47 segments/3 mice; $p < 0.001$, MWU), layer I apical dendrites (controls = 2.6 [2.3–3.2] per 10 µm, n = 24 segments/3 mice; 6-OHDA = 1.7 [1.3–3.1] per 10 µm, n = 25 segments/3 mice; $p = 0.02$, MWU), but no changes in layer II/III spine density (controls = 3.6 [2.8–4.4] per 10 µm, 6-OHDA = 3.5 [3.0–4.2] per 10 µm, n = 36 segments/3 mice for each group, $p = 0.6$, MWU). **H-I**) Representative confocal images of biocytin-filled PT neurons from controls (H) and 6-OHDA mice (I). **J-K**) Representative confocal images of segments of dendrites from controls (**J**) and 6-OHDA mice (K), as indicated by the green boxes in (H-I). **L**) Summarized results showing decreased spine densities of layer V basal dendrites (control = 5.2 [3.7–6.4] per 10 µm, n = 34 segments/3 mice; 6-OHDA = 3.2 [2.7–4.0] per 10 µm, n = 40 segments/3 mice; $p < 0.001$, MWU), layer I apical dendrites (controls = 3.6 [2.9–4.6] per 10 µm, n = 24 segments/3 mice; 6-OHDA = 2.0 [1.3–2.5] per 10 µm, n = 24 segments/3 mice; $p < 0.001$, MWU), but no changes in layer II/III spine density (controls = 3.8 [3.0–4.8] per 10 µm, n = 24 segments/3 mice; 6-OHDA = 4.0 [3.1–4.7] per 10 µm, n = 22 segments/3 mice; $p = 0.6$, MWU).

To interrogate postsynaptic structural changes associated with DA depletion, we injected either AAVrg-eGFP into the pontine nuclei to label M1 PT neurons using eGFP (**Figure 3D-G**), or Retrobeads into the pontine nuclei followed by *ex vivo* biocytin filling via patch pipettes for morphology studies (**Figure 3H-L**). The density of dendritic spines of PT neurons across M1 layers were assessed in controls and 6-OHDA mice. Experiments using two different experimental approaches showed consistent results. Specifically, the spine density of the basal dendrites in layer V and the apical dendrites in layer I from 6-OHDA mice decreased significantly relative to those from controls (**Figure 3E-G, J-L**). This is consistent with the preferential motor thalamic projections to layers I and V (*5*, *8*, *24*). In contrast, the spine density of apical dendrites of PT neurons in layer II/III was not altered following the loss of SNc DA neurons (**Figure 3G, L**). These data are consistent with the unaltered SC-PT excitation in 6-OHDA mice (**Figures 1, 2**) and the earlier reports showing preferential sensory cortical projections to layer II/III (*8*). For comparison, AAVrg-eGFP labeled IT neurons showed no change in the spine density of either basal or apical dendrites across cortical layers (**Figure S4**). Thus, SNc DA degeneration induces loss of dendritic spines of PT neurons those are mainly targeted by the thalamic inputs, but not those targeted by sensory inputs. The presynaptic and postsynaptic morphological changes further support our hypothesis that selective impairments of thalamocortical synapses onto M1 PT neurons occur in parkinsonism.

SNc DA degeneration decreases the effectiveness of thalamic driving of M1 PT neuronal firing

As reported in the somatosensory cortex (*35*), optogenetically synchronized mTh excitation could effectively drive M1 PT neuronal firing in control animals, which was mediated by both AMPA and NMDA receptors (Rs) (**Figure S5A-B**). Following SNc DA neurodegeneration, the composition of glutamatergic receptors at the thalamo-PT synapses, measured as the NMDA/AMPA ratio, was not altered (**Figure S5C-D**), indicating that synchronous thalamic excitation remains capable to drive PT neuronal firing.

Given the prevalence of abnormally synchronized thalamocortical activity in parkinsonism (*16*, *36*, *37*), it is therefore plausible to hypothesize that thalamic inputs drive the aberrant pattern of PT neuronal activity through the strengthened remaining thalamo-PT connections at dendrites and spines, the excitability of which cannot be accurately measured using whole-cell voltage-clamp recordings. To assess this possibility, we recorded retrogradely labeled PT and IT neurons under current-clamp mode and compare the effectiveness of thalamic and cortical inputs in driving neuronal firing in both control and 6-OHDA mice. A 20-Hz optogenetic stimulation (1 ms duration) was delivered to activate ChR2-expressed thalamic or sensory cortical axons in M1.

The effectiveness of thalamic driving of PT neuronal firing decreased significantly in slices from 6-OHDA mice relative to those from controls, as reflected by fewer APs per stimulation and a decreased AP firing probability (**Figure 4A-C**). In contrast, we did not detect alterations in the effectiveness of thalamo-IT or SC-PT synaptic driving of neuronal firing between groups (**Figure 4D-F, G-I**). Consistent with the input- and cell-subtype-specific changes in synaptic strength, these data further suggest that loss of DA selectively disrupts the functional connectivity between the motor thalamus and PT

neurons. The results also suggest that monosynaptic thalamic inputs are not sufficient to synchronize PT neuronal firing in bursts under parkinsonian state.

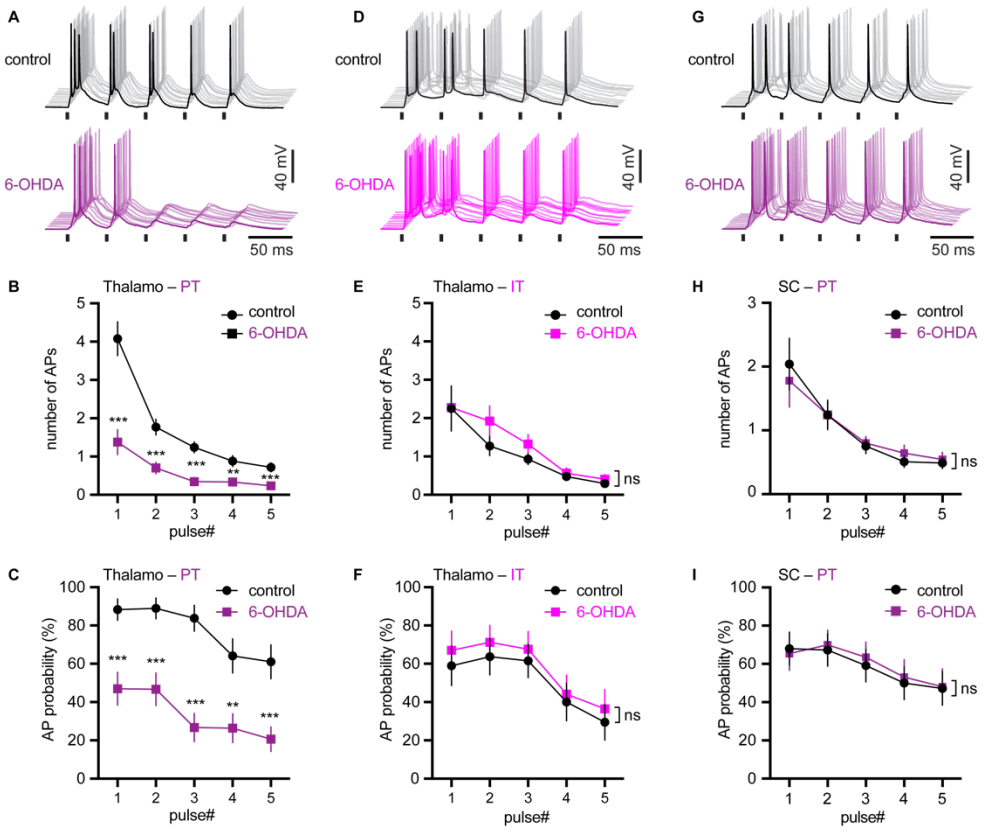

Figure 4. **SNc DA degeneration decreases the effectiveness of thalamic driving of M1 PT neuronal firing**. **A**) Representative traces of AP firing of M1 PT neurons from controls and 6-OHDA mice in response to 20 Hz optogenetic stimulation of thalamocortical inputs. AP traces from 10 trials were aligned for both groups. **B-C**) Summarized results show that both the number (B) and probability (C) of synaptically-generated APs in M1 PT neurons decreased significantly in 6-OHDA mice relative to controls. Mixed effects model followed by Sidak's tests, $p < 0.0001$ for group difference. Control = 29 neurons/3 mice; 6-OHDA = 33 neurons/4 mice. **D**) Representative traces of AP firing of M1 IT neurons from controls and 6-OHDA mice in response to 20 Hz optogenetic stimulation of thalamocortical inputs. **E-F**) Summarized results show that the number (E) and probability (F) of synaptically-generated APs in M1 IT neurons was not altered in 6-OHDA mice relative to controls. Mixed effects model, $p = 0.56$ for group difference on AP probability; $p = 0.36$ for group difference on the number of APs; control = 19 neurons/3 mice; 6-OHDA = 19 neurons/3 mice. **G**) Representative traces of AP firing of M1 PT neurons from controls and 6-OHDA mice in response to 20 Hz optogenetic stimulation of sensory cortical inputs. **H-I**) Summarized results show that both the number (H) and probability (I) of synaptically-generated APs in M1 PT neurons upon stimulation of cortical inputs were not altered in 6-OHDA mice relative to controls. Mixed effects model, $p = 0.76$ for group difference on AP probability; $p = 0.97$ for group difference on the number of APs; control = 25 neurons/3 mice; 6-OHDA = 26 neurons/3 mice. Light intensity was 2.3 mW/mm^2 for all patterning experiments. Short vertical bars in (A, D, G) indicate the period when optical stimulation was delivered.

Distinct composition of glutamatergic receptors at thalamic and sensory cortical inputs to M1 PT neurons

NMDARs are critical for thalamocortical synaptic integration and plasticity and contribute to pathological processes in neurological disorders. Thus, we assessed whether NMDARs activation mediates the selective impairment of thalamo-PT inputs, but not the thalamo-IT or SC-PT synapses, following the loss of DA. Specifically, we found that the NMDA/AMPA ratio at the thalamo-PT synapses, relative to thamamo-IT synapses and SC-PT synapses, was significantly higher (**Figure 5A, B**). These data indicate that NMDARs are functionally enriched at thalamo-PT synapses relative to SC-PT or thalamo-IT synapses. In addition, there was a stronger inward rectification of AMPARs at SC-PT synapses relative to thalamic projections to PT or IT neurons (**Figure 5A, C**). These data indicate that GluA2-lacking, Ca^{2+}-permeable AMPARs are enriched at SC-PT synapses relative to those from the motor thalamus to M1 PT or IT neurons in control mice.

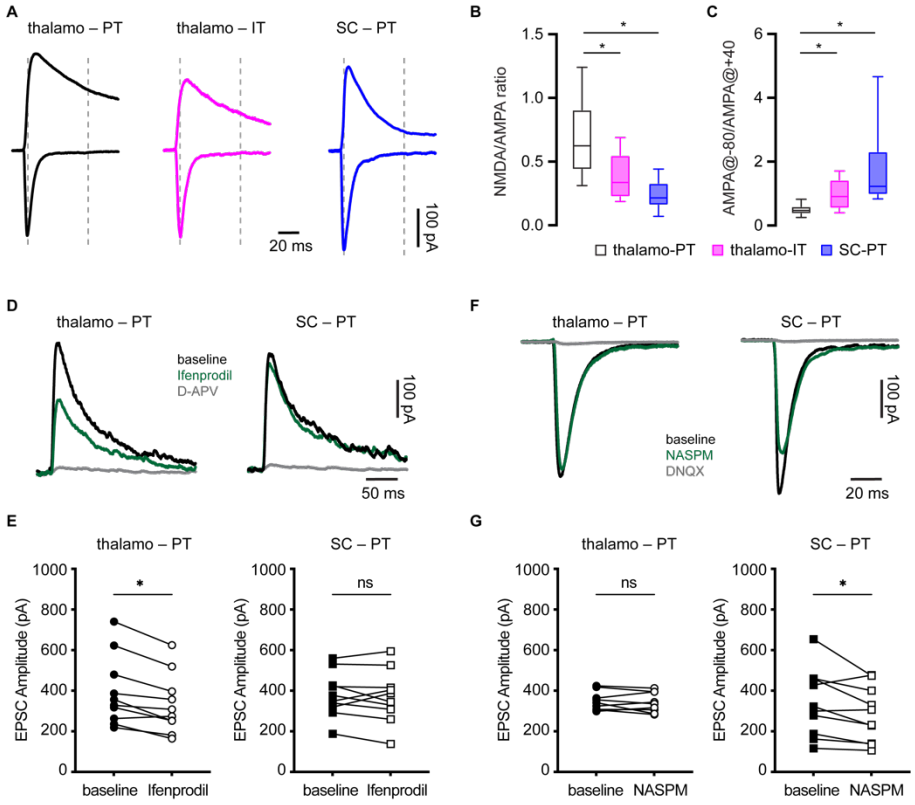

Figure 5. **Distinct postsynaptic receptor properties at thalamic and sensory cortical inputs to PT neurons**. **A**) Representative traces of AMPARs- and NMDARs-mediated responses from different synapses in M1. **B-C**) Box plots showing differences in NMDA/AMPA ratios (B, thalamo-PT synapses = 0.62 [0.44–0.91], n = 34 neurons/4 mice; thalamo-IT synapse = 0.34 [0.22–0.55], n = 19 neurons/3 mice; SC-PT synapses = 0.22 [0.16–0.33], n = 25 neurons/3 mice; $p < 0.0001$; Kruskal-Wallis test followed by Dunn's test) and AMPARs rectification properties (C, thalamo-PT synapses = 0.47 [0.37–0.60], n = 34 neurons/4 mice; thalamo-IT synapse = 0.91 [0.54–1.4], n = 25 neurons/3 mice; SC-PT synapses = 1.23 [0.97–2.32], n = 19 neurons/3 mice; $p < 0.0001$; Kruskal-Wallis test followed by Dunn's test) of different synapses in M1. **D-E**) Pharmacology studies showing different sensitivities of NMDARs-mediated transmission at thalamic and sensory cortical synapses to ifenprodil. (D) Representative traces of isolated NMDARs-mediated EPSCs at +40 mV from thalamo-PT and SC-PT synapses at baseline, in ifenprodil, and in ifenprodil plus D-APV. (E) Connected symbols showing the effects of ifenprodil to the amplitude of NMDARs-mediated EPSCs at thalamo-PT (left, baseline = 342 [256–516] pA, ifenprodil = 292 [234–428] pA; n = 10 neurons/4 mice; $p = 0.004$, WSR) and SC-PT (right, baseline = 363 [313–452] pA, ifenprodil = 366 [296–443] pA; n = 10 neurons/3 mice; $p = 0.6$, WSR) synapses. **F**) Representative traces of AMPARs-mediated EPSCs from thalamo-PT and SC-PT synapses at baseline, in NASPM, and in NASPM plus DNQX. **G**) Connected symbols showing the effects of NASPM to the amplitude of AMPARs-mediated EPSCs at thalamo-PT (left, baseline = 333 [305–378] pA; NASPM = 327 [301–395] pA; n = 10 neurons/ 4 mice; $p = 0.6$, WSR) and SC-PT synapses (right, baseline = 311 [181–459] pA; NASPM = 269 [106–419] pA; n = 10 neurons/ 4 mice; $p = 0.02$, WSR). WSR, Wilcox signed rank test.

Next, we used a pharmacological approach to further confirm the input-specific composition of glutamatergic receptors in PT neurons. A large body of evidence suggests that GluN2B subunit-containing NMDA receptors with larger Ca^{2+} conductance enriched at thalamocortical synapses in the prefrontal cortex and play a critical role in pathological processes in neurological diseases (*38*, *39*). Consistently, a noncompetitive antagonist of GluN2B-containing NMDARs ifenprodil (3 μM) significantly and consistently reduced the amplitude of NMDARs-EPSCs at thalamo-PT synapses, but did not produce consistent effect to the NMDARs-EPSCs amplitude of SC-PT synapses (**Figure 5D, E**). In addition, to quantitively assess the functional contribution of GluA2-lacking, Ca^{2+}-permeable AMPARs at different inputs, a selective antagonist 1-naphthyl acetyl spermine trihydrochloride (NASPM) was used. Bath application of NASPM (100 μM) consistently decreased the amplitude of AMPARs-EPSCs of SC-PT synapses but did not produce significant effect to AMPARs-EPSCs at thalamo-PT synapses (**Figure 5F, G**).

Together, we conclude that GluN2B-containing NMDARs are enriched at thalamo-PT synapses, and that GluA2-lacking, Ca^{2+}-permeable AMPARs functionally contribute more to SC-PT transmission in physiological state.

NMDARs mediate the decreased thalamocortical transmission to M1 PT neurons

Next, given the enrichment of NMDARs at thalamo-PT synapses, we further assessed if NMDARs activation mediates the decreased thalamo-PT synaptic strength in parkinsonism. Studies, including our own recent work, report that activation of NMDARs by exogenously application of NMDA is sufficient to mimic NMDAR-dependent pathological processes in basal ganglia nuclei (*33*, *40*, *41*). When we incubated brain

slices with exogenous NMDA (25 μM) for 1 hour, the treatment did not decrease cell density of M1 or affect the cellular excitability of PT neurons (**Figure S6**), indicating that the NMDA treatment was not excitotoxic (*33*). Brain slices from controls and 6-OHDA mice were then incubated with (1) normal ACSF, (2) NMDA-containing ACSF (25 μM), or (3) D-APV/NMDA-containing ACSF for one hour (*33*), prior to physiological and anatomical studies (**Figure 6A**). In brain slices from vehicle-injected control mice, *ex vivo* NMDA incubation reduced the amplitude of thalamo-PT oEPSCs but did not alter NMDA/AMPA ratio and AMPA rectification index at thalamo-PT synapses (**Figure 6B, D**). The suppression of thalamo-PT oEPSCs by NMDA treatment could be abolished by D-APV co-incubation (**Figure S7**). In addition, *ex vivo* NMDA incubation did not alter the amplitude of thalamo-IT oEPSCs (**Figure S8**), further arguing for a synapse- and cell-subtype specific effect of the NMDA treatment. Altogether, these data indicate that NMDARs stimulation induces synapse- and cell subtype-specific changes in M1 circuits and that such specificity might be due to compartment-specific expression of NMDAR subunits (**Figure 5**).

If NMDARs and the associated signaling cascade become activated upon loss of SNc DA neurons, contributing to the reduced thalamo-PT excitation, a corollary would be that the effects of *ex vivo* NMDARs stimulation to thalamo-PT oEPSCs (**Figure 6B, D**) should be occluded in slices from 6-OHDA mice. Consistently, *ex vivo* NMDA incubation had no effect to the amplitude of thalamo-PT oEPSCs from 6-OHDA mice (**Figure 6C, E**). These data suggest that excessive NMDARs activation is sufficient to decrease the thalamic excitation to PT neurons from control mice, and that the associated signaling

cascade likely mediates the reduced thalamic excitation to PT neurons *in vivo* following DA depletion.

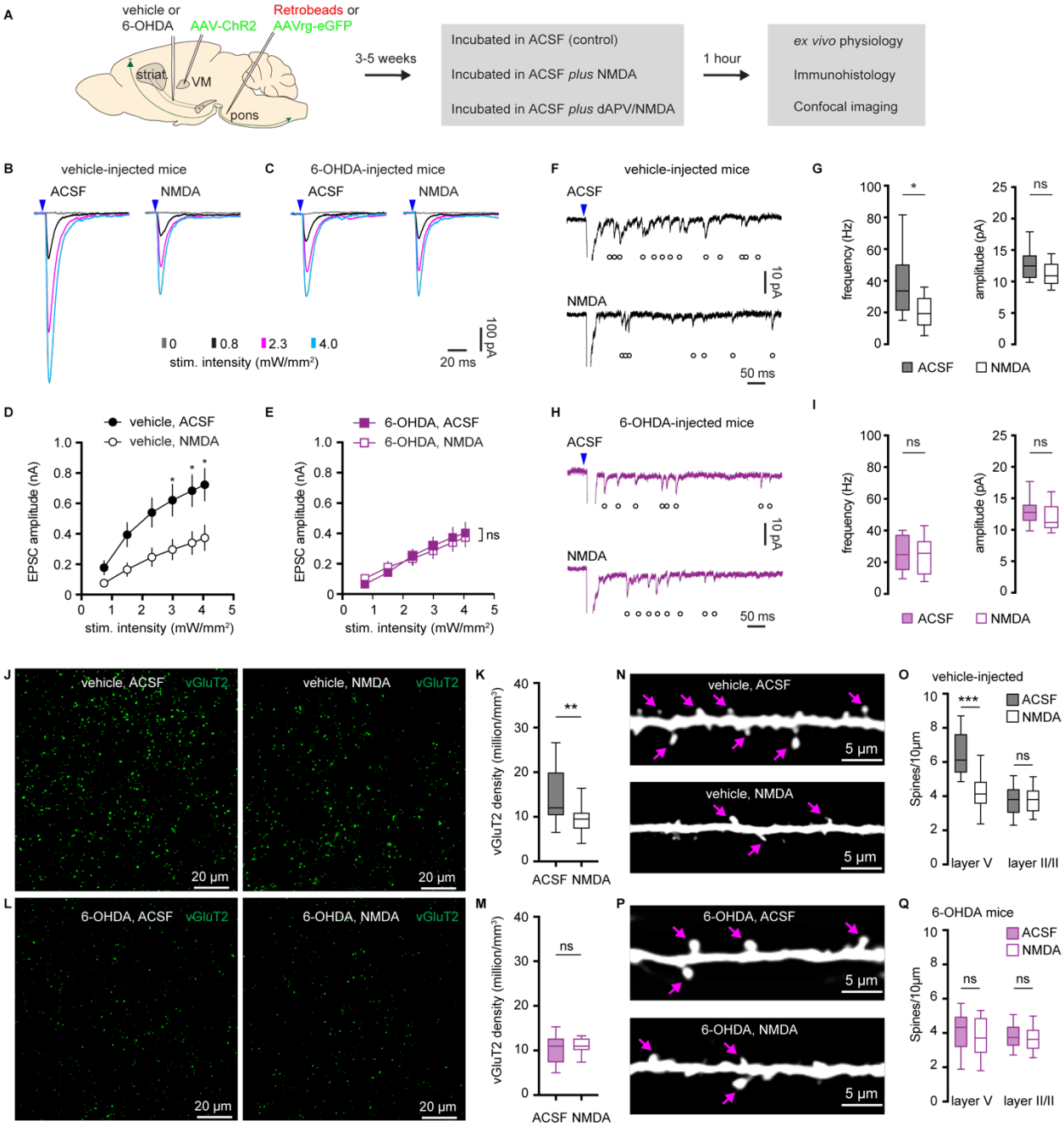

Figure 6. **Excessive NMDARs activation mediates the impaired thalamo-PT transmission after DA depletion**. **A**) Experimental design. **B-C**) Representative traces of optogenetically-evoked thalamo-PT EPSCs from vehicle-injected controls (B) and 6-OHDA-injected mice (C), which were either incubated in normal ACSF (control) or ACSF containing NMDA. **D-E**) Summarized results show that NMDA incubation decreased the amplitude of oEPSCs from vehicle-injected controls (D, group effect, $p < 0.0001$, mixed effects model followed by Sidak's tests), but not those from 6-OHDA-injected mice (E, group effect, $p > 0.79$, mixed effects model). **F-G**) NMDA incubation decreased the frequency but not the amplitude of optogenetically-evoked Sr^{2+}-EPSCs from vehicle-injected controls. **F**) Representative traces of Sr^{2+}-EPSCs. **G**) Summarized results (frequency of Sr^{2+}-EPSCs in vehicle-injected mice, control = 33.6 [21.1–50.4] Hz, n = 24 neurons/3 mice; NMDA = 10.9 [9.6–12.9] pA; n = 24 neurons/3 mice; $p = 0.001$, MWU; amplitude of Sr^{2+}-EPSCs in vehicle-injected mice, control = 12.5 [10.5–14.2] pA, n = 24 neurons/3 mice; NMDA = 19.4 [11.8–29.2] Hz, n = 24 neurons/3 mice; $p = 0.1$, MWU). **H-I**) NMDA incubation did not alter the frequency or the amplitude of optogenetically-evoked Sr^{2+}-EPSCs from 6-OHDA-injected mice. **H**) Representative traces of Sr^{2+}-EPSCs. **I**) Summarized results (frequency of Sr^{2+}-EPSCs in 6-OHDA mice, control = 24.8 [15–37.4] Hz, n = 17 neurons/3 mice; NMDA = 25.6 [12.2–33.4] pA, n = 17 neurons/3 mice; $p = 0.6$, MWU; amplitude of Sr^{2+}-EPSCs in 6-OHDA mice; control = 12.9 [11.3–14.0] pA, n = 17 neurons/3 mice; NMDA = 11.2 [10.3–13.8] Hz, n = 27 neurons/3 mice; $p = 0.21$, MWU). **J**) Representative confocal images of vGluT2 immunoreactivity from ACSF- and NMDA-treated slices of controls. **K**) Box plot shows that NMDA incubation reduced vGluT2 densities in slices of controls (ACSF = 12 [10–14.8] million/mm^3, n = 20 samples/3 mice; NMDA = 9 [7–10.8] million/mm^3, n = 16 samples/3 mice; $p = 0.0016$, MWU). **L**) Representative confocal images of vGluT2 immunoreactivity from ACSF- and NMDA-treated slices of 6-OHDA. **M**) Box plot shows that NMDA incubation did not affect vGluT2 densities in slices of 6-OHDA mice (ACSF = 11 [8–12] million/mm^3, 20 samples/3 mice; NMDA = 11 [9–12] million/mm^3, 20 samples/3 mice; $p = 0.7$, MWU). **N**) Representative confocal images of dendritic spines in layer V from ACSF- and NMDA-treated slices of controls. **O**) Box plot shows that NMDA incubation reduced layer V spine densities in slices of controls (ACSF = 6 [5.4–7.6] spines/10 μm, n = 24 samples/3 mice; and NMDA = 4.1 [3.5–4.9] spines/10 μm, n = 25 samples/3 mice; $p < 0.0001$, MWU), but did not alter the spine density of apical dendrites in layer II/III (ACSF = 3.8 [3–4.4] spines/10 μm; NMDA = 3.8 [3.1–4.3] spines/10 μm; 36 samples/3 mice for each group; $p = 0.7$, MWU). **P**) Representative confocal images of M1 layer V dendritic spines from ACSF- and NMDA-treated slices of 6-OHDA mice. **Q**) Box plot shows that NMDA incubation did not alter layer V or II/III spine densities in slices from 6-OHDA mice (layer V: ACSF = 4.3 [3.2–5] spines/10 μm, n = 29 samples/3 mice; NMDA = 3.7 [2.8–4.9] spines/10 μm, n = 31 samples/3 mice; $p = 0.4$, MWU; layer II/III: ACSF = 3.7 [3.2–4.4] spine/10 μm; NMDA = 3.6 [3.1–4.2] spines/10 μm, 36 samples/3 mice for each group; $p = 0.45$, MWU). Arrows in (N and P) indicate representative spines on dendrites.

Loss of DA decreases the number of functional thalamocortical connections to PT neurons (**Figures 2-3**). Thus, we further studied the impact of exogenous NMDA incubation on Sr^{2+}-induced quantal glutamate release at thalamocortical synapses to PT neurons. In slices from vehicle-injected controls, NMDA incubation significantly decreased the frequency, but not the amplitude of optogenetically evoked thalamo-PT

Sr^{2+}-EPSCs (**Figure 6F, G**). In contrast, in slices from 6-OHDA mice, NMDA incubation did not alter the frequency or the amplitude of optogenetically-evoked thalamo-PT Sr^{2+}-EPSCs (**Figure 6H, I**). The above data suggest that NMDARs activation reduces the number of functional thalamocortical inputs to M1 PT neurons, but this effect was occluded in 6-OHDA mice.

Next, we studied whether *ex vivo* NMDA incubation would induce structural changes at thalamo-PT synapses. A separate set of brain slices from controls and 6-OHDA mice were incubated with ACSF or NMDA-containing ACSF for 1 hour and then fixed with 4% PFA for immunohistochemistry studies. We found that *ex vivo* NMDA incubation robustly decreased vGluT2 densities in layer V of M1 of controls, relative to those incubated in ACSF (**Figure 6J, K**). However, NMDA incubation did not alter vGluT2 densities in layer V from 6-OHDA mice relative to those treated with normal ACSF (**Figure 6L, M**). Postsynaptically, NMDA incubation decreased the spine densities of basal dendrites in layer V of retrogradely labeled PT neurons in controls but did not alter the spine density of apical dendrites in layer II/III (**Figure 6N, O**). In 6-OHDA mice, *ex vivo* NMDA incubation did not alter spine densities of PT neurons in either layer V or layer II/III (**Figure 6P, Q**). Altogether, our physiological and anatomical results suggest that excessive NMDARs activation is sufficient to decrease thalamocortical connection to M1 PT neurons, and that the NMDARs-mediated mechanisms are synapse-specific, likely underlying the decreased thalamic excitation to PT neurons in 6-OHDA mice.

Disruption of basal ganglia outputs rescues the decreased thalamocortical transmission in parkinsonism

Next, we attempted to understand the interaction between M1 adaptations and the abnormal BG output in parkinsonism. Given that disrupting BG output by dopaminergic medications or functional surgery effectively improves motor function in both PD subjects and parkinsonian animals (*42–44*), it has been proposed that prevention of abnormal BG activity from propagating to the downstream motor regions (e.g., the thalamocortical network) would allow them to perform normal function in motor control and there be beneficial (*45*, *46*). Therefore, we suppressed the SNr output using chemogenetic approaches to assess how such manipulation affected thalamocortical adaptations in both controls and DA-depleted mice.

Because parvalbumin (PV)-expressing GABAergic neurons account for majority of SNr projection neurons (*7*), we unilaterally injected PV-Cre knock-in mice with vehicle or 6-OHDA into the MFB, plus AAV9-hSyn-FLEX-hM4Di-mCherry into the SNr of the same hemisphere to chemogenetically manipulate of basal ganglia outputs (**Figure 7A**). Immunofluorescence staining showed the selective expression of hM4Di (Gi)-DREADDS-mCherry in SNr PV-expressing cells (**Figure 7A**) and a preferred projection of mCherry-labeled axon terminals in the VM motor thalamus (**Figure 7D**). There was no difference in the number of hM4Di-expressing cells in the SNr between 6-OHDA mice and controls. Bath application of DREADDS agonist CNO (10 μM) effectively suppressed the frequency of autonomous firing of SNr neurons from 6-OHDA mice (**Figure 7B, C**) as well as the frequency of spontaneous inhibitory postsynaptic currents (sIPSCs) of VM thalamic neurons (**Figure 7D-F**).

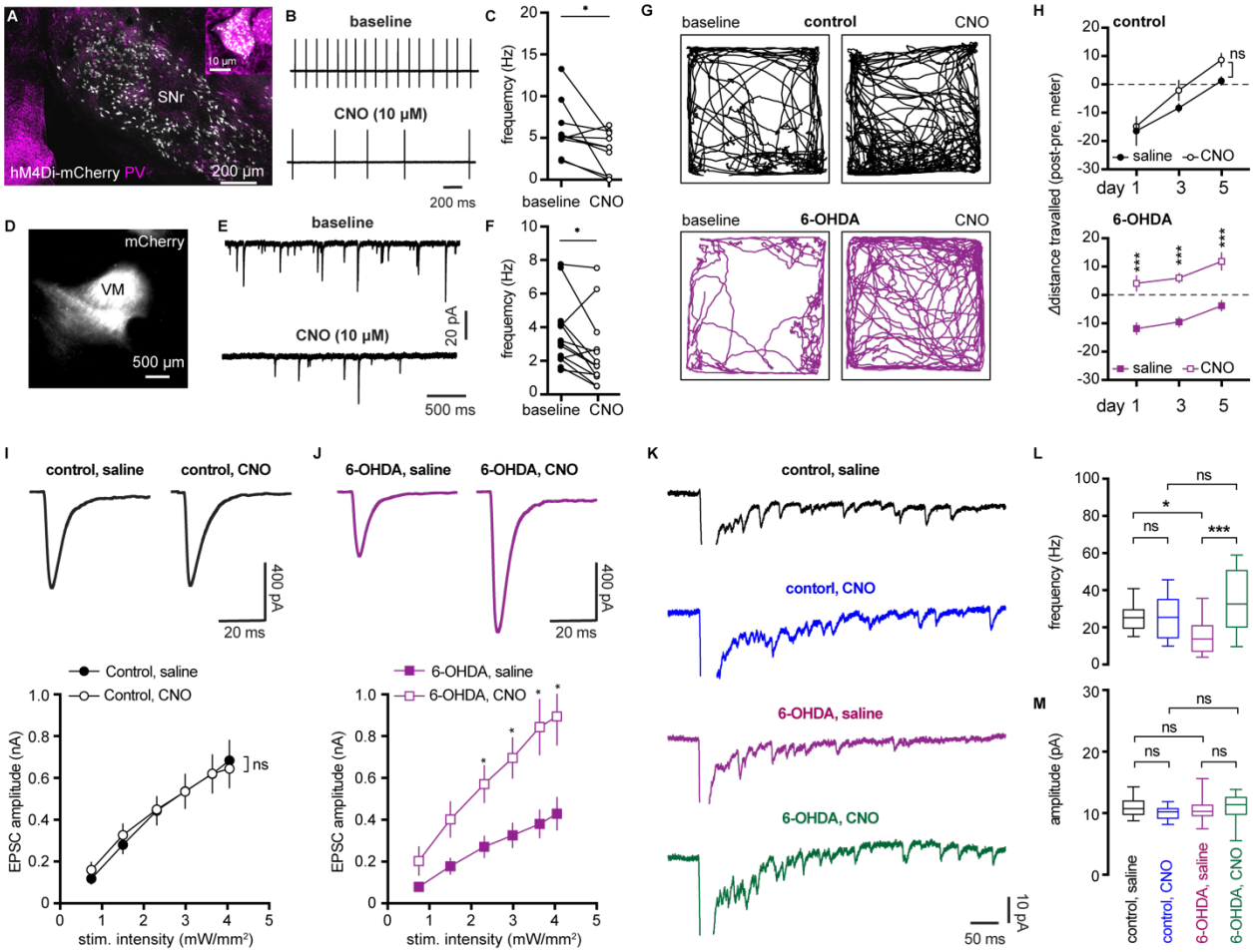
A
SNr
10 µm
hM4Di-mCherry PV
200 µm
B
baseline
CNO (10 µM)
200 ms
C
frequency (Hz)
baseline CNO
D
mCherry
VM
500 µm
E
baseline
CNO (10 µM)
20 pA
500 ms
F
frequency (Hz)
baseline CNO
G
baseline control CNO
baseline 6-OHDA CNO
H
control
saline CNO
day 1 3 5
6-OHDA
Δdistance travelled (post-pre, meter)
I
control, saline
control, CNO
400 pA
20 ms
Control, saline
Control, CNO
EPSC amplitude (nA)
stim. intensity (mW/mm²)
J
6-OHDA, saline
6-OHDA, CNO
K
control, saline
contorl, CNO
6-OHDA, saline
6-OHDA, CNO
10 pA
50 ms
L
frequency (Hz)
M
amplitude (pA)
control, saline
control, CNO
6-OHDA, saline
6-OHDA, CNO

Figure 7. **Disrupting Basal ganglia output rescues thalamocortical adaptations following loss of SNc DA neurons**. **A**) Representative confocal images showing hM4Di-mCherry expression in the PV-expressing SNr neurons. *Inset*, image under high magnification. Similar number of SNr neurons were infected between groups (controls = 276 [160–357] neurons/slice, n = 20 slices/10 mice; 6-OHDA = 233 [170–271] neurons/slice, n = 23 slices/12 mice; p = 0.08, MWU). **B**) Representative traces of the autonomous firing of a SNr neuron from a DA-depleted mouse prior to and after CNO application. **C**) hM4Di activation by CNO (10 μM) effectively suppressed the *ex vivo* autonomous firing of SNr neurons (baseline = 5.2 [4.3–7.5] Hz, CNO = 3.9 [0.27–5.6] Hz; n = 10 neurons/3 mice; p = 0.02, WSR). **D**) Representative image showing mCherry-labeled SNr axonal projections to the VM thalamus. **E-F**) hM4Di activation by CNO effectively reduced the frequency of sIPSCs of VM thalamic neurons (baseline = 3.1 [2.1–4.3] Hz, CNO = 1.7 [1.1–3.2] Hz; n = 13 neurons/3 mice; p = 0.02, WSR). (**E**, examples; **F**, summarized results). **G**) Representative track plots showing the effects of CNO injections to locomotor activity of controls and 6-OHDA mice in an open field on day 5. **H**) Summarized results showing the difference of distance travelled in an open field arena between pre- and post-saline/CNO injections in controls and 6-OHDA mice. Behavioral tested were conducted on days 1, 3 and 5. **I-J**) hM4Di activation did not alter the amplitude of optogenetically-evoked thalamocortical EPSCs in PT neurons from controls (I, p = 0.9, mixed effects model), but increased the amplitude of optogenetically-evoked thalamocortical EPSCs in PT neurons from 6-OHDA mice (J, p = 0.007, mixed effects model followed by Sidak's test). *Top*, representative traces of oEPSCs in PT neurons; *bottom*, summarized results. 18-24 neurons from 3-4 mice for each group. **K**) Representative traces of optogenetically-evoked Sr^{2+}-EPSCs in controls and 6-OHDA mice treated with saline or CNO. **L**) Summarized results showing CNO injection did not alter the frequency of Sr^{2+}-EPSCs in slices from controls (control/saline = 25 [19–30] Hz, control/CNO = 25 [14–35] Hz; $p > 0.9$), but decreased the frequency of Sr^{2+}-EPSCs in slices from 6-OHDA mice (6-OHDA/saline = 13.8 [6.7–21.3] Hz, 6-OHDA/CNO = 32.4 [19.6–50.8] Hz, p = 0.0001). **M**) Summarized results showing CNO injection did not alter the amplitude of Sr^{2+}-EPSCs in slices from either controls (control/saline = 10.7 [9.7–12.1] pA, n= 18 neurons/3 mice; control/CNO = 10.2 [9.1–10.9] pA, n = 18 neurons/3 mice; p = 0.8) or 6-OHDA mice (6-OHDA/saline = 10.3 [9.5–11.4] pA, n= 22 neurons/3 mice; 6-OHDA/CNO = 11.4 [9.7–12.7] pA, n = 19 neurons/3 mice; p = 0.95). Kruskal-Wallis test followed by Dunn's tests.

PV-Cre mice with SNr hM4Di expression in PV-expressing SNr neurons were subcutaneously injected with either CNO (1.0 mg/kg, at 12 hrs interval between injections) or saline for 5 consecutive days to continuously disrupt the abnormal basal ganglia outputs, or control for subcutaneous injections, respectively. Open field locomotor activities were measured on days 1, 3 and 5. Difference in the total distance travelled prior to and post injections were comparable between CNO-injected and saline-injected control mice (**Figure 7G, H**). This is perhaps because that CNO's effects to unilateral SNr neuronal activity of DA intact mice were not sufficient to robustly affect general motor

activity. As predicted, CNO injection significantly increased the locomotor activity of 6-OHDA mice relative to saline-injected mice (**Figure 7G, H**). These data indicate that the SNr output was effectively suppressed by hM4Di activation in 6-OHDA mice, leading to behavioral improvements (*47*, *48*). The improved locomotor activity following the SNr suppression has been reported to be mediated by disinhibiting pedunculopontine nucleus (PPN) (*49*). Given the extensive SNr collateral projections to the PPN and the motor thalamus (*7*), it is reasonable to speculate that hM4Di activation could also disrupt GABAergic transmission from the SNr to the motor thalamus, which is also supported by CNO-induced reduction of sIPSCs frequency recorded from the VM motor thalamic neurons (**Figure 7D-F**).

To determine whether disruption of pathological BG inputs to the mTh could rescue adaptive changes of M1 circuits, the same cohort of mice described above also received retrobeads injection into the pons to retrogradely label M1 PT neurons and ChR2(H134R)-eYFP injection into the mTh for optogenetic stimulation of thalamo-PT synapses. In vehicle-injected control mice, we found that chemogenetic suppression of SNr activity through repetitive CNO injection did not alter the amplitude of optogenetically evoked thalamo–PT oEPSCs (**Figure 7I**). In contrast, repetitive CNO injection significantly increased the amplitude of optogenetically evoked thalamo–PT oEPSCs in 6-OHDA mice (**Figure 7J**).

Further, we assessed the effects of chemogenetic suppression of SNr activity to quantal properties of thalamocortical transmission to PT neurons. Chemogenetic suppression of SNr activity through repetitive CNO injection did not alter either the frequency or the amplitude of optogenetically-evoked Sr^{2+}-EPSCs at the thalamo–PT

synapses of vehicle-injected control mice (**Figure 7K-M**). In contrast, repetitive CNO injection significantly increased the frequency, but not the amplitude, of optogenetically evoked Sr^{2+}-EPSCs at the thalamo–PT synapses of 6-OHDA mice (**Figure 7K-M**). Together, these data indicate that chemogenetic suppression of basal ganglia outputs can rescue the decreased thalamo-PT synaptic transmission in 6-OHDA mice.

Discussion

The present study provides novel insights into motor cortical circuitry adaptations following the degeneration of SNc DA neurons. First, we demonstrated that DA depletion induces cell-subtype- and input-specific downregulation of thalamic excitation to M1 PT neurons (**Figure 1**). Physiological and anatomical analyses showed that the weakened thalamocortical synaptic strength is likely associated with fewer thalamocortical connections (**Figure 2–4**). Moreover, NMDARs are enriched at thalamocortical synapses to PT neurons (**Figure 5**). Prolonged NMDARs activation *ex vivo* was sufficient to decrease thalamocortical excitation to M1 PT neurons from control animals, but such effects were occluded in 6-OHDA mice (**Figure 6**). These data suggest that excessive NMDARs activation *in vivo* is perhaps involved in mediating the decreased thalamocortical transmission after DA depletion. In addition, chemogenetic suppression of SNr activity can reverse the disrupted thalamo-PT synaptic transmission in parkinsonian mice (**Figure 7**), suggesting that disrupting pathological BG output has the potential to rescue cortical circuitry dysfunction in parkinsonism.

Considering the complexity of cortical circuit and its plasticity mechanisms, the impact of BG dysfunction on M1 outputs should be more complicated than it has been proposed. Consistently, relative to IT neurons, PT neurons are functionally more vulnerable to DA degeneration and their activities are robustly entrained by the pathological oscillations through the transition of the motor thalamus (*12*, *16*, *21*, *25*, *26*, *37*). We also have demonstrated a series of intrinsic (*26*) and thalamocortical adaptations in M1 of parkinsonian mice, mainly affecting PT neurons. Thus, both intrinsic and synaptic adaptations can contribute to an impaired thalamic driving of cortical PT neuronal firing,

leading to a reduced motor cortical outputs and impaired motor control in parkinsonian state (*12*, *14*, *17*, *21*, *30*, *50*, *51*).

Although the PT and IT neurons in M1 differ in their gene expression, morphology, and electrophysiological properties (*52*–*54*), the AMPAR-mediated excitatory inputs from the motor thalamus to them are comparable in healthy animals (*8*). Thus, we posited that additional cellular and circuit mechanisms are involved and contribute to cell-subtype-selective changes in parkinsonian state. Accordingly, we found that a greater contribution of GluN2B-NMDARs to thalamo-PT transmission could be a critical mechanism, which may explain (1) the selective weakening of thalamo-PT synaptic strength (**Figure 1**) and (2) the selective loss of spines in layer V, but not in layer II/III, in slices from 6-OHDA mice (**Figure 3**) or control slices with NMDARs stimulation (**Figure 6**), as well as (3) the unaltered thalamo-IT connections in slices prepared from 6-OHDA mice (**Figure 1**) or slices from controls with NMDARs stimulation (**Figure S8**).

Our work demonstrates distinct levels of GluN2B-NMDARs at thalamic *versus* sensory cortical inputs to M1 PT neurons. Interestingly, this compartment- and input-specific expression of NMDARs at glutamatergic inputs to cortical neurons (i.e., pyramidal neurons or interneurons) has been reported (*55*–*57*). Earlier *in vivo* studies also indicated input-specific recruitments of AMPARs and NMDARs in mediating excitatory transmission of motor cortical PT neurons (*58*). Importantly, the selective alterations of glutamatergic inputs to M1 in parkinsonism are consistent with findings from MPTP-treated parkinsonian monkeys, showing that abnormal loss of glutamatergic axon terminals in M1 selectively occurs in thalamocortical system, but not within the cortico-cortical projections (*24*).

Overstimulation of GluN2B-NMDARs by the excessive glutamate could be a key molecular mechanism underlying the weakened thalamo-PT synaptic connection in parkinsonism. M1 receives convergent glutamatergic projections from several cortical areas and subcortical regions (*8*). In parkinsonism, pathological patterns of pyramidal neuronal activity (e.g., enhanced burst firing) and synchronous glutamatergic inputs (e.g., thalamic afferents) are expected to significantly elevate local glutamate concentration (*16*, *35*, *37*), which in turn leads to GluN2B-NMDARs overstimulation and the associated signaling cascades (*33*, *55*, *59*, *60*), such as the ubiquitin-proteasome pathway (*59*, *61*), or cathepsin B-like protease activity that regulates actin-based cytoskeleton to mediate morphological changes (*62*). It is worth noting that adaptive changes at the distal dendrites of the layer I were not properly assessed in current physiology studies due to the limitations of experimental approaches and therefore future work is needed to explore this area using complementary approaches (e.g., voltage imaging technologies).

Impaired DA neuromodulation in M1 may also play a role in cortical dysfunction in PD (*63*). However, the mesocortical DA projections mainly arise from the ventral tegmental area in rodents (*64*), which are less affected in the model used in the present study. Also, the reduced thalamo-PT transmission could be rescued by chemogenetic suppression of BG output in DA-depleted mice. Thus, it is unlikely that the partial loss of DA neuromodulation in M1 plays a dominant role in the observations described in the present study. In contrast, the abnormal BG outputs might be the major pathological signals underlying the impaired cortical dysfunction and parkinsonian motor impairments. Of interests, chemogenetic suppression of BG outputs in DA-depleted animals could restore some aspects of thalamocortical function and this finding could shed light on the

circuit mechanisms underlying the symptomatic alleviation mediated by dopaminergic medications and functional surgery that occurs in PD (*45*, *46*).

Conclusion

Altogether, we demonstrated that degeneration of SNc DA neurons triggers cell-subtype- and input-specific adaptations in M1. While the present study focuses on thalamocortical synaptic adaptations and potential molecular mechanisms, future studies remain needed to explore adaptive changes in the motor cortex and understand their roles in PD pathophysiology and treatment.

Materials and Methods

Animals

Wild-type (WT) C57BL/6J mice of both sexes (3–4 month-old, RRID:IMSR_JAX:000664) were obtained from the Van Andel Institute vivarium internal colony and used in the study. Homozygous PV-Cre knock-in mice were originally purchased from Jackson laboratories (stock# 017320RRID: IMSR_JAX:017320, Bar Harbor, ME) and maintained at a C57/BL6J background in Van Andel Institute vivarium. Mouse genotyping was conducted through the service of Transnetyx, Inc (Cordova, TN). Mice were housed up to four animals per cage under a 12/12 h light/dark cycle with access to food and water *ad libitum* in accordance with NIH guidelines for care and use of animals. All animal studies were reviewed and approved by the Institutional Animal Care and Use Committee at Van Andel Institute (reference#: 22-02-006).

Stereotaxic surgery for 6-OHDA and virus injections

Mice were randomly assigned to different treatment groups. Mice were mounted and secured in a stereotaxic frame (Kopf) under 2% isoflurane anesthesia. Throughout the procedure, body temperature of the mouse was maintained by a thermostatic heating pad. Once the skull was opened, small holes were drilled above the pre-determined targets to inject: 1) 6-OHDA (3–4 µg) into the medial forebrain bundle (MFB, from bregma (in mm), anterior-posterior (AP) = -0.7, mediolateral (ML) = +1.2, and dorsoventral (DV) = -4.7 from the brain surface) to induce unilateral degeneration of nigrostriatal pathway, or vehicle into the MFB to serve as vehicle-injected controls; 2) retrobeads (200 nl, 10x dilution) into the ipsilateral pontine nuclei (from bregma (in mm), AP = -5.0, ML = +0.6, DV = -5.0) or

contralateral striatum (from bregma (in mm), AP = +0.2, ML = -2.3, DV = -2.9) to retrogradely label PT and IT neurons, respectively; and 3) AAV9-hSyn-ChR2(H134R)-eYFP (RRID:Addgene_127090, 300 nl at a titer of $3.6x10^{12}$ GC/ml) into the ventral subregion of the motor thalamus (from bregma (in mm), AP = -1.6, ML = 0.8, DV = -4.3) to label thalamocortical axon terminals for optogenetics studies. *Post hoc* histology analysis showed that the AAV infected most of the ventral medial and ventral anteriolateral thalamus (VM/VAL, Figure 1). A small cohort of mice also received pAAV9-hSyn-DIO-hM4D(Gi)-mCherry (RRID:Addgene_44362, 300 nl at a titer of $2.2x10^{12}$ GC/ml) injection into the substantia nigra pars reticulata (from bregma (in mm), AP = -3.4, ML = +1.4, DV = -4.6) for chemogenetic studies. For morphology studies, AAVrg-hSyn-eGFP (RRID:Addgene_50465, 300 nl at $2x10^{13}$ GC/ml) were injected into the pontine nuclei to retrogradely label PT neuron in the motor cortex. All injection were performed using a 10 µl syringe (Hamilton, Reno, NV) mounted on a motorized microinjector (Stoelting, Wood Dale, IL) at a speed of 100 nl/min. Details of the stereotaxic injection procedure can be found on Protocol.io (dx.doi.org/10.17504/protocols.io.rm7vzye28lx1/v1)

Slice preparation for electrophysiology

3–4 weeks post-injections, brain slices were prepared for electrophysiology. Mice were anesthetized with avertin (250–300 mg/kg), followed by transcardial perfusion with ice-cold sucrose-based artificial cerebrospinal fluid (aCSF) equilibrated with 95% O_2/5% CO_2 and containing (in mM): 230 sucrose, 26 $NaHCO_3$, 10 glucose, 10 MgSO4, 2.5 KCl, 1.25 NaH_2PO_4, 0.5 $CaCl_2$, 1 sodium pyruvate and 0.005 L-glutathione. Coronal brain sections (250 µm) containing the primary motor cortex were prepared using a vibratome (VT1200s,

Leica, RRID:SCR_018453) in the same sucrose-based solution that was maintained at ~4 °C using a recirculating chiller (FL300, Julabo, Allentown, PA). Slices were then held in aCSF equilibrated with 95% O_2/5% CO_2 and containing (in mM): 126 NaCl, 26 $NaHCO_3$, 10 glucose, 2 $MgSO_4$, 2.5 KCl, 1.25 NaH_2PO_4, 1 sodium pyruvate and 0.005 L-glutathione at 35 °C for 30 min for recovery and then at room temperature until electrophysiology recordings or NMDA incubation. Details of slice preparation can be found on Protocols.io (dx.doi.org/10.17504/protocols.io.36wgqj2eovk5/v1)

Brain slice physiology and optogenetics

Brain slices were placed in recording chamber with continuous perfusion of recording solution containing (in mM): 126 NaCl, 26 $NaHCO_3$, 10 glucose, 3 KCl, 1.6 $CaCl_2$, 1.5 $MgSO_4$, and 1.25 NaH_2PO_4. The solution was equilibrated with 95% O_2/5%CO_2 and maintained at 33–34°C using feedback controlled in-line heater (TC-324C, Warner Instruments). To assess synaptic strength, TTX (1 μM) and 4-AP (100 μM) were routinely included to isolate optogenetically evoked monosynaptic thalamocortical or corticocortical EPSCs in M1. To test the effectiveness of thalamic and cortical driving of M1 neuronal firing (Figure 4), TTX/4-AP were omitted from the recording solution and a selective $GABA_A$ receptor antagonist SR-95531 (GABAzine) was added to prevent the recruitment of GABAergic inhibitions. Neurons were visualized using a CCD camera (SciCam Pro, Scientifica, UK) and SliceScope Pro 6000 system (Scientifica, UK) integrated with a BX51 upright microscope and motorized micromanipulators. Retrogradely labelled neurons in the layer V were targeted under a 60x water immersion objective lens (Olympus, Japan) for whole-cell patch clamp recording using a MultiClamp 700B amplifier

(RRID:SCR_018455) and Digidata 1550B controlled by pClamp 11 software (Molecular Devices, San Jose, CA; RRID:SCR_011323). Data were sampled at 50 KHz. Borosilicate glass pipettes (O.D. = 1.5 mm, I.D. = 0.86 mm, length = 10 cm, item#: BF150-86-10, Sutter Instruments, Novato, CA) were pulled by micropipette puller (P1000, Sutter instrument, Novato, CA; RRID:SCR_021042) and used for patch clamp recording with a resistance of 3–6 MOhm when filled with (1) Cs-methanesulfonate-based internal solution of (in mM): 120 CH_3O_3SCs, 2.8 NaCl, 10 HEPES, 0.4 Na_4-EGTA, 5 QX314-HBr, 5 phosphocreatine, 0.1 spermine, 4 ATP-Mg, and 0.4 GTP-Na (pH 7.3, 290 mOsm); or (2) K-gluconate based internal solution, containing (in mM): 140 K-gluconate, 3.8 NaCl, 1 $MgCl_2$, 10 HEPES, 0.1 Na_4-EGTA, 2 ATP-Mg, and 0.1 GTP-Na (pH 7.3, 290 mOsm). Biocytin (0.2%) was added to the K-gluconate-based internal solution to fill Retrobeads-labeled PT neurons (~ 30 min), and the morphology of the filled neuron was revealed using Cy5-conjugated streptavidin. Spontaneous inhibitory postsynaptic currents from the motor thalamic neurons were conducted in the presence of glutamatergic receptor blockers (i.e., 50 μM D-APV and 20 μM DNQX) under whole-cell voltage-clamp mode (at -70 mV) using a high Cl^- internal solution, containing (in mM): 135 CsCl, 3.6 NaCl, 1 $MgCl_2$, 10 HEPES, 0.1 Na_4-EGTA, 2 ATP-Mg, and 0.1 GTP-Na (pH 7.3, 290 mOsm). Optogenetic stimulation was delivered using a 478 nm LED (pE-300^{Ultra}, CoolLED, UK; RRID:SCR_021972) through a 60x water immersion objective lens (Olympus), centering at the site of patched neurons with a field of illumination of ~ 450 μm in diameter. In chemogenetics studies, water soluble clozapine-n-oxide (CNO, 10 μM, HelloBio# HB6149) was applied *ex vivo* to test hM4Di activation on SNr neuronal firing or sIPSCs in the VM thalamic neurons. The effects of CNO on neuronal firing or sIPSCs were

assessed 15-20 min after the start of CNO perfusion. Electrophysiology data were analyzed and quantified using Clampfit 11.1 (Molecular Devices, San Jose, CA; RRID:SCR_011323) and Minianalysis 6.0.3 (Synaptosoft, USA; RRID:SCR_002184). Peak amplitude of AMPARs-mediated EPSCs at -80 mV was quantified as a measure of synaptic strength. To calculate NMDA/AMPA ratio, amplitude of NMDA-mediated currents at +40 mV was measured at 50 ms post-optogenetic stimulation when AMPARs EPSCs largely decay to baseline level. Details of brain slice physiology and optogenetics can be found at Protocols.io (dx.doi.org/10.17504/protocols.io.eq2ly7m2rlx9/v1).

Immunohistochemistry

Brain tissues after electrophysiology or NMDA incubation (1 hour) were fixed in 4% PFA in 0.1 M phosphate buffer overnight at 4 °C and then were resected into 70–100 μm slices using a VT1000s vibratome (Leica Biosystems, Deer Park, IL; RRID:SCR_016495) to prepare brain sections for immunohistochemistry of tyrosine hydroxylase (TH) or NeuN. In vGluT2 stereology and neuronal morphology studies, mice were perfused with ice-cold phosphate-buffered saline (PBS, pH = 7.4) for 5 min and subsequently with 4% PFA mice for 30 min. The brain was then extracted and saved in 4% PFA overnight at 4 °C before being resected into 70 μm slices using a VT1000s vibratome (Leica Biosystems, Deer Park, IL; RRID:SCR_016495) for immunohistochemistry or morphology studies.

Brain slices were rinsed 3x with PBS before being incubated with 0.2% Triton X-100 and 2% normal donkey serum (Sigma-Aldrich) for 60 min at room temperature. Brain slices were then incubated with primary antibodies, including mouse anti-TH (1:2000, cat# MAB318, MilliporeSigma; RRID:AB_2201528), or anti-NeuN (MAB377, MilliporeSigma,

RRID:AB_2298772), guinea pig anti-vGluT2 (cat# 135404, Synaptic Systems, RRID:AB_887884) for 48 hours at 4 °C or overnight at room temperature. Sections were then rinsed 3x with PBS and incubated with secondary antibodies for 90 min, including donkey anti-mouse Alexa Fluor 488 (Cat# 715-545-150; Jackson ImmunoResearch Labs, West Grove, PA; RRID:AB_2340846), donkey anti-mouse Alexa Fluor 594 (Cat# 715-585-150; Jackson ImmunoResearch Labs, West Grove, PA; RRID:AB_2340854), or donkey anti-guinea pig Alexa Fluor 488 (Cat# 706-545-148; Jackson ImmunoResearch Labs, West Grove, PA; RRID:AB_2340472), at room temperature before washing with PBS for 3 times. Brain sections were mounted with VECTASHIELD antifade mounting medium (Cat# H-1000, Vector Laboratories, Newark, CA; RRID:AB_2336789), were cover-slipped and sealed with nail polish. Details of IHC protocol can be found at Protocols.io (dx.doi.org/10.17504/protocols.io.6qpvr417ogmk/v1). TH- and vGluT2-immunoreactivity (ir) was imaged under 20x or 40x objective lens using an Olympus DP80 camera through an Olympus BX63F microscope, or a confocal laser scanning microscope (A1R, Nikon, Japan; RRID:SCR_020317). TH-ir of control and 6-OHDA mice was quantified by normalizing the striatal TH-ir from the ipsilateral side to the value from the contralateral hemisphere, with a subtraction of background measured from the cerebral cortex. Details of immunohistochemical quantification of TH signals can be found at Protocols.io (dx.doi.org/10.17504/protocols.io.n2bvj85qngk5/v1).

Animal behavior

To assess parkinsonian motor deficits, mice were subject to 1) open field locomotion test, where their locomotor activity and rotations were monitored for 10 min and quantified

using Anymaze software (Stoelting, Wood Dale, IL; https://www.any-maze.com/); (2) cylinder test using a 600-ml glass beaker to assess the spontaneous forelimbs use during weight-bearing touches which were recorded using a digital camcorder at 60 fps (Panasonic, HC-V180K) and analyzed off-line by a researcher blinded to treatments. 3 weeks post-surgery, vehicle- or 6-OHDA-injected mice received subcutaneous saline- or water-soluble clozapine-n-oxide (CNO, 1 mg/kg body weight, catalogue # HB6149, HelloBio, Princeton, NJ) injections for chemogenetic studies. The injections were conducted at 7 am and 7 pm each day for 5 consecutive days. Locomotion tests (10 min) were performed 30 min after subcutaneous injections on days 1, 3 and 5 to measure the behavioral effects. Following behavioral tests, animals were used to prepare brain slices for physiology studies. All physiology recordings were started ~3 hours post saline or CNO injections. Details of locomotion and cylinder tests can be found at Protocols.io (dx.doi.org/10.17504/protocols.io.e6nvwjxmdlmk/v1,
and dx.doi.org/10.17504/protocols.io.eq2ly7m9qlx9/v1).

Validation of mouse model of parkinsonism

To confirm a complete degeneration of nigrostriatal DA pathway in 6-OHDA mice, animals were subject to behavioral tests at 3 weeks post-surgery, prior to electrophysiology and anatomy experiments (*26*). Relative to controls, 6-OHDA mice showed a significantly reduced locomotor activity in an open field arena (distance travelled in 10 min, control = 39 [33–48] m, n = 51 mice; 6-OHDA = 21 [15–27] m, n = 52 mice; $p < 0.0001$, MWU test). Moreover, 6-OHDA mice also exhibited asymmetric forelimb use in cylinder test (% of ipsilateral forelimb use, controls = 50 [49–52]%, n = 51 mice; 6-OHDA = 85 [79–93]%, n

= 52 mice; $p < 0.0001$, MWU test). *Post hoc* immunostaining of striatal TH was conducted, which showed a > 80% loss of striatal TH immunoreactivity (TH-ir) in the lesioned hemisphere of 6-OHDA mice (%$TH_{ipsilateral/contralateral\ striatum}$, control = 100 [97–102]%, n = 51 mice; 6-OHDA = 11 [7–16]%, n = 52 mice; $p < 0.0001$, MWU test). Procedures of TH quantification and behavioral validation of parkinsonism can be found on Protocols.io (dx.doi.org/10.17504/protocols.io.n2bvj85qngk5/v1, dx.doi.org/10.17504/protocols.io.e6nvwjxmdlmk/v1, and dx.doi.org/10.17504/protocols.io.eq2ly7m9qlx9/v1).

Confocal imaging and digital image analysis

vGluT2-ir was collected from layers V under a 100x objective lens using a Nikon A1R confocal microscope. Z stack Images with a 0.15 μm interval were taken under the identical settings, including laser power, gain, pinhole size, and scanning speed etc. between animals. The density of vGluT2-ir was estimated based on the immunostaining signals between 5 and 8 μm below the surface of slices using the optical dissector method (*65*). To assess the density of neurons in layer V, NeuN-ir was collected using a 40x objective lens (1024 X1024 pixels; z step = 1 μm, Nikon A1R) followed by stereology analysis. For spine density analysis and dendritic examination, segments of basal dendrites were tracked down from the cell bodies of retrogradely labeled PT neurons in M1 and imaged under an oil-immersion 100x objective using the confocal microscope (NA = 1.45; x/y, 1024 X 1024 pixels; z step = 0.5 μm, A1R, Nikon). The distance from the soma to the basal dendrites analyzed was 50–100 μm. eGFP- or biocytin-labeled segments of the apical dendrites were selected from the layer I and II/III. To quantify spine

density, only microscopic image data with ample eGFP expression and high signal-to-noise ratios were included. Spine density analysis was performed using Imaris software (version 9.3, Oxford, UK; RRID:SCR_007370). Briefly, 2-3 dendritic segments from the targeted layers measuring 20–30 microns in length were reconstructed three-dimensionally using Imaris' filament tracer function from each confocal image. Spines were then manually traced, reconstructed, and quantified. For accurate three-dimensionally reconstruction, both the dendrite segments and spines were recomputed automatically based on the manual traces. Details of imaging process can be found at Protocols.io (dx.doi.org/10.17504/protocols.io.3byl4jmxzlo5/v1).

Statistics

Statistics analysis was performed in GraphPad Prism 9 (GraphPad Software, San Diego, CA; RRID:SCR_002798). Nonparametric Mann-Whitney U (MWU) test, Wilcox signed rank (WSR) test, and Kruskal–Wallis test followed by Dunn's Multiple Comparisons (as indicated in the text) were used to compare the medians of 2 or 3 groups in order to minimize the assumption of dataset normality. For experiments with nested design wherein more than one cells were sampled from each animal, a mixed effects model was used to compare group difference where the responses (e.g., EPSCs amplitude) were modeled as a combination of a fixed effect (i.e., vehicle versus 6-OHDA injections; or saline versus CNO injections) and random effects associated with each animal. Behavioral results in the Figure 7 were analyzed using repeated measures two-way ANOVA. Whenever applicable, *post hoc* Šídák's multiple comparisons test was performed. Data were collected from 3-8 mice per study. Individual animals were considered independent samples. All statistic tests were two tailed with p values < 0.05

(*), 0.01 (**), or 0.001 (***) as thresholds for statistical significance. Data are reported as median plus interquartile ranges (in square brackets).

Data availability. The datasets analyzed during the current study are available at: https://osf.io/m9dyw/?view_only=c96a43dbe04c4acf95c04c3cc7059ae5.

References cited

1. R. L. Albin, A. B. Young, J. B. Penney, The functional anatomy of basal ganglia disorders. *Trends Neurosci*. 12, 366–375 (1989).

2. A. Galvan, T. Wichmann, Pathophysiology of parkinsonism. *Clin Neurophysiology Official J Int Fed Clin Neurophysiology*. 119, 1459–74 (2008).

3. M. M. McGregor, A. B. Nelson, Circuit mechanisms of Parkinson's disease. *Neuron*. 101, 1042–1056 (2019).

4. K. C. Nakamura, A. Sharott, P. J. Magill, Temporal Coupling with Cortex Distinguishes Spontaneous Neuronal Activities in Identified Basal Ganglia-Recipient and Cerebellar-Recipient Zones of the Motor Thalamus. *Cereb Cortex*. 24, 81–97 (2014).

5. E. Kuramoto, T. Furuta, K. C. Nakamura, T. Unzai, H. Hioki, T. Kaneko, Two Types of Thalamocortical Projections from the Motor Thalamic Nuclei of the Rat: A Single Neuron-Tracing Study Using Viral Vectors. *Cereb Cortex*. 19, 2065–2077 (2009).

6. Á. L. Bodor, K. Giber, Z. Rovó, I. Ulbert, L. Acsády, Structural correlates of efficient GABAergic transmission in the basal ganglia–thalamus pathway. *J Neurosci*. 28, 3090–3102 (2008).

7. L. E. McElvain, Y. Chen, J. D. Moore, G. S. Brigidi, B. L. Bloodgood, B. K. Lim, R. M. Costa, D. Kleinfeld, Specific populations of basal ganglia output neurons target distinct brain stem areas while collateralizing throughout the diencephalon. *Neuron*. 109, 1721-1738.e4 (2021).

8. B. M. Hooks, T. Mao, D. A. Gutnisky, N. Yamawaki, K. Svoboda, G. M. G. Shepherd, Organization of Cortical and Thalamic Input to Pyramidal Neurons in Mouse Motor Cortex. *J Neurosci*. 33, 748–760 (2013).

9. M. Gaidica, A. Hurst, C. Cyr, D. K. Leventhal, Distinct Populations of Motor Thalamic Neurons Encode Action Initiation, Action Selection, and Movement Vigor. *J Neurosci*. 38, 6563–6573 (2018).

10. C. Bosch-Bouju, B. I. Hyland, L. C. Parr-Brownlie, Motor thalamus integration of cortical, cerebellar and basal ganglia information: implications for normal and parkinsonian conditions. *Front Comput Neurosc*. 7, 163 (2013).

11. N. Takahashi, S. Moberg, T. A. Zolnik, J. Catanese, R. N. S. Sachdev, M. E. Larkum, D. Jaeger, Thalamic input to motor cortex facilitates goal-directed action initiation. *Curr Biol*. 31, 4148-4155.e4 (2021).

12. F. Aeed, N. Cermak, J. Schiller, Y. Schiller, Intrinsic Disruption of the M1 Cortical Network in a Mouse Model of Parkinson's Disease. *Movement Disord*. 36, 1565–1577 (2021).

13. B. I. Hyland, S. Seeger-Armbruster, R. A. Smither, L. C. Parr-Brownlie, Altered recruitment of motor cortex neuronal activity during the grasping phase of skilled reaching in a chronic rat model of unilateral Parkinsonism. *J Neurosci*. 39, 0720–19 (2019).

14. B. Pasquereau, M. R. DeLong, R. S. Turner, Primary motor cortex of the parkinsonian monkey: altered encoding of active movement. *Brain*. 139, 127–143 (2016).

15. C. Bosch-Bouju, R. A. Smither, B. I. Hyland, L. C. Parr-Brownlie, Reduced Reach-Related Modulation of Motor Thalamus Neural Activity in a Rat Model of Parkinson's Disease. *J Neurosci*. 34, 15836–15850 (2014).

16. E. Brazhnik, A. J. McCoy, N. Novikov, C. E. Hatch, J. R. Walters, Ventral Medial Thalamic Nucleus Promotes Synchronization of Increased High Beta Oscillatory Activity in the Basal Ganglia–Thalamocortical Network of the Hemiparkinsonian Rat. *J Neurosci*. 36, 4196–4208 (2016).

17. B. A. Sauerbrei, J.-Z. Guo, J. D. Cohen, M. Mischiati, W. Guo, M. Kabra, N. Verma, B. Mensh, K. Branson, A. W. Hantman, Cortical pattern generation during dexterous movement is input-driven. *Nature*. 577, 386–391 (2020).

18. K. V. Shenoy, M. Sahani, M. M. Churchland, Cortical Control of Arm Movements: A Dynamical Systems Perspective. *Annu Rev Neurosci.* 36, 337–359 (2012).

19. A. P. Georgopoulos, A. F. Carpenter, Coding of movements in the motor cortex. *Curr Opin Neurobiol*. 33, 34–39 (2015).

20. M. R. DeLong, Primate models of movement disorders of basal ganglia origin. *Trends Neurosci*. 13, 281–285 (1990).

21. B. Pasquereau, R. S. Turner, Primary motor cortex of the parkinsonian monkey: differential effects on the spontaneous activity of pyramidal tract-type neurons. *Cereb Cortex*. 21, 1362–1378 (2011).

22. J. A. Goldberg, T. Boraud, S. Maraton, S. N. Haber, E. Vaadia, H. Bergman, Enhanced Synchrony among Primary Motor Cortex Neurons in the 1-Methyl-4-Phenyl-1,2,3,6-Tetrahydropyridine Primate Model of Parkinson's Disease. *J Neurosci*. 22, 4639–4653 (2002).

23. L. Guo, H. Xiong, J.-I. Kim, Y.-W. Wu, R. R. Lalchandani, Y. Cui, Y. Shu, T. Xu, J. B. Ding, Dynamic rewiring of neural circuits in the motor cortex in mouse models of Parkinson's disease. *Nat Neurosci*. 18, 1299–1309 (2015).

24. R. M. Villalba, J. A. Behnke, J.-F. Pare, Y. Smith, Comparative Ultrastructural Analysis of Thalamocortical Innervation of the Primary Motor Cortex and Supplementary Motor Area in Control and MPTP-Treated Parkinsonian Monkeys. *Cereb Cortex* (2021), doi:10.1093/cercor/bhab020.

25. O. K. Swanson, R. Semaan, A. Maffei, *Eneuro*, in press, doi:10.1523/eneuro.0548-19.2021.

26. L. Chen, S. Daniels, Y. Kim, H.-Y. Chu, Cell Type-Specific Decrease of the Intrinsic Excitability of Motor Cortical Pyramidal Neurons in Parkinsonism. *J Neurosci*. 41, 5553–5565 (2021).

27. A. R. Brown, B. Hu, M. C. Antle, G. C. Teskey, Neocortical movement representations are reduced and reorganized following bilateral intrastriatal 6-hydroxydopamine infusion and dopamine type-2 receptor antagonism. *Exp Neurol*. 220, 162–170 (2009).

28. R. Viaro, M. Morari, G. Franchi, Progressive motor cortex functional reorganization following 6-hydroxydopamine lesioning in rats. *J Neurosci*. 31, 4544–4554 (2011).

29. E. K. Plowman, N. J. Thomas, J. A. Kleim, Striatal Dopamine Depletion Induces Forelimb Motor Impairments and Disrupts Forelimb Movement Representations within the Motor Cortex. *J Park Dis*. 1, 93–100 (2011).

30. J. S. Biane, Y. Takashima, M. Scanziani, J. M. Conner, M. H. Tuszynski, Thalamocortical Projections onto Behaviorally Relevant Neurons Exhibit Plasticity during Adult Motor Learning. *Neuron*. 89, 1173–1179 (2016).

31. L. Petreanu, D. Huber, A. Sobczyk, K. Svoboda, Channelrhodopsin-2–assisted circuit mapping of long-range callosal projections. *Nat Neurosci*. 10, 663–668 (2007).

32. A. Rios, S. Soma, J. Yoshida, S. Nonomura, M. Kawabata, Y. Sakai, Y. Isomura, *Eneuro*, in press, doi:10.1523/eneuro.0110-19.2019.

33. H.-Y. Chu, E. L. McIver, R. F. Kovaleski, J. F. Atherton, M. D. Bevan, Loss of hyperdirect pathway cortico-subthalamic inputs following degeneration of midbrain dopamine neurons. *Neuron*. 95, 1306-1318.e5 (2017).

34. J. Ding, J. D. Peterson, D. J. Surmeier, Corticostriatal and Thalamostriatal Synapses Have Distinctive Properties. *J Neurosci*. 28, 6483–6492 (2008).

35. R. M. Bruno, B. Sakmann, Cortex Is Driven by Weak but Synchronously Active Thalamocortical Synapses. *Science*. 312, 1622–1627 (2006).

36. A. Oswal, P. Brown, V. Litvak, Synchronized neural oscillations and the pathophysiology of Parkinson's disease. *Curr Opin Neurol*. 26, 662–670 (2013).

37. K. C. Nakamura, A. Sharott, T. Tanaka, P. J. Magill, Input Zone-Selective Dysrhythmia in Motor Thalamus after Dopamine Depletion. *J Neurosci*. 41, 10382–10404 (2021).

38. O. H. Miller, A. Bruns, I. B. Ammar, T. Mueggler, B. J. Hall, Synaptic Regulation of a Thalamocortical Circuit Controls Depression-Related Behavior. *Cell Reports*. 20, 1867–1880 (2017).

39. H. Wang, G. G. Stradtman, X.-J. Wang, W.-J. Gao, A specialized NMDA receptor function in layer 5 recurrent microcircuitry of the adult rat prefrontal cortex. *Proc National Acad Sci*. 105, 16791–16796 (2008).

40. E. L. McIver, J. F. Atherton, H.-Y. Chu, K. E. Cosgrove, J. Kondapalli, D. Wokosin, D. J. Surmeier, M. D. Bevan, Maladaptive downregulation of autonomous subthalamic nucleus activity following the loss of midbrain dopamine neurons. *Cell Reports*. 28, 992-1002.e4 (2019).

41. J. F. Atherton, E. L. McIver, M. R. Mullen, D. L. Wokosin, D. J. Surmeier, M. D. Bevan, Early dysfunction and progressive degeneration of the subthalamic nucleus in mouse models of Huntington's disease. *Elife*. 5, e21616 (2016).

42. R. Levy, J. O. Dostrovsky, A. E. Lang, E. Sime, W. D. Hutchison, A. M. Lozano, Effects of Apomorphine on Subthalamic Nucleus and Globus Pallidus Internus Neurons in Patients With Parkinson's Disease. *J Neurophysiol*. 86, 249–260 (2001).

43. M. Filion, L. Tremblay, P. J. Be´dard, Effects of dopamine agonists on the spontaneous activity of globus pallidus neurons in monkeys with MPTP-induced parkinsonism. *Brain Res*. 547, 145–149 (1991).

44. M. Merello, J. Balej, M. Delfino, A. Cammarota, O. Betti, R. Leiguarda, Apomorphine induces changes in GPi spontaneous outflow in patients with parkinson's disease. *Mov. Disord.* 14, 45–49 (1999).

45. J. A. Obeso, M. Jahanshahi, L. Alvarez, R. Macias, I. Pedroso, L. Wilkinson, N. Pavon, B. Day, S. Pinto, M. C. Rodríguez-Oroz, J. Tejeiro, J. Artieda, P. Talelli, O. Swayne, R. Rodríguez, K. Bhatia, M. Rodriguez-Diaz, G. Lopez, J. Guridi, J. C. Rothwell, What can man do without basal ganglia motor output? The effect of combined unilateral subthalamotomy and pallidotomy in a patient with Parkinson's disease. *Exp Neurol*. 220, 283–292 (2009).

46. T. Wichmann, Changing views of the pathophysiology of Parkinsonism. *Mov. Disord.* 34, 1130–1143 (2019).

47. J. Kim, Y. Kim, R. Nakajima, A. Shin, M. Jeong, A. H. Park, Y. Jeong, S. Jo, S. Yang, H. Park, S.-H. Cho, K.-H. Cho, I. Shim, J. H. Chung, S.-B. Paik, G. J. Augustine, D. Kim, Inhibitory Basal Ganglia Inputs Induce Excitatory Motor Signals in the Thalamus. *Neuron*. 95, 1181-1196.e8 (2017).

48. S. Seeger-Armbruster, C. Bosch-Bouju, S. T. C. Little, R. A. Smither, S. M. Hughes, B. I. Hyland, L. C. Parr-Brownlie, Patterned, But Not Tonic, Optogenetic Stimulation in Motor Thalamus Improves Reaching in Acute Drug-Induced Parkinsonian Rats. *J Neurosci*. 35, 1211–1216 (2015).

49. T. K. Roseberry, A. M. Lee, A. L. Lalive, L. Wilbrecht, A. Bonci, A. C. Kreitzer, Cell-Type-Specific Control of Brainstem Locomotor Circuits by Basal Ganglia. *Cell*. 164, 526–537 (2016).

50. L. Wang, J. M. Conner, J. Rickert, M. H. Tuszynski, Structural plasticity within highly specific neuronal populations identifies a unique parcellation of motor learning in the adult brain. *Proc National Acad Sci*. 108, 2545–2550 (2011).

51. R. Hasegawa, T. Ebina, Y. R. Tanaka, K. Kobayashi, M. Matsuzaki, Structural dynamics and stability of corticocortical and thalamocortical axon terminals during motor learning. *Plos One*. 15, e0234930 (2020).

52. B. A. Suter, M. Migliore, G. M. G. Shepherd, Intrinsic electrophysiology of mouse corticospinal neurons: a class-specific triad of spike-related properties. *Cereb Cortex*. 23, 1965–1977 (2013).

53. G. M. G. Shepherd, Corticostriatal connectivity and its role in disease. *Nat Rev Neurosci*. 14, 278–291 (2013).

54. H. Peng, P. Xie, L. Liu, X. Kuang, Y. Wang, L. Qu, H. Gong, S. Jiang, A. Li, Z. Ruan, L. Ding, Z. Yao, C. Chen, M. Chen, T. L. Daigle, R. Dalley, Z. Ding, Y. Duan, A. Feiner, P. He, C. Hill, K. E. Hirokawa, G. Hong, L. Huang, S. Kebede, H.-C. Kuo, R. Larsen, P. Lesnar, L. Li, Q. Li, X. Li, Y. Li, Y. Li, A. Liu, D. Lu, S. Mok, L. Ng, T. N. Nguyen, Q. Ouyang, J. Pan, E. Shen, Y. Song, S. M. Sunkin, B. Tasic, M. B. Veldman, W. Wakeman, W. Wan, P. Wang, Q. Wang, T. Wang, Y. Wang, F. Xiong, W. Xiong, W. Xu, M. Ye, L. Yin, Y. Yu, J. Yuan, J. Yuan, Z. Yun, S. Zeng, S. Zhang, S. Zhao, Z. Zhao, Z. Zhou, Z. J. Huang, L. Esposito, M. J. Hawrylycz, S. A. Sorensen, X. W. Yang, Y. Zheng, Z. Gu, W. Xie, C. Koch, Q. Luo, J. A. Harris, Y. Wang, H. Zeng, Morphological diversity of single neurons in molecularly defined cell types. *Nature*. 598, 174–181 (2021).

55. O. H. Miller, A. Bruns, I. B. Ammar, T. Mueggler, B. J. Hall, Synaptic Regulation of a Thalamocortical Circuit Controls Depression-Related Behavior. *Cell Reports*. 20, 1867–1880 (2017).

56. M. Lafourcade, M.-S. H. van der Goes, D. Vardalaki, N. J. Brown, J. Voigts, D. H. Yun, M. E. Kim, T. Ku, M. T. Harnett, Differential dendritic integration of long-range inputs in association cortex via subcellular changes in synaptic AMPA-to-NMDA receptor ratio. *Neuron* (2022), doi:10.1016/j.neuron.2022.01.025.

57. E. M. Lewis, H. E. Spence, N. Akella, A. Buonanno, Pathway-specific contribution of parvalbumin interneuron NMDARs to synaptic currents and thalamocortical feedforward inhibition. *Mol Psychiatr*. 27, 5124–5134 (2022).

58. K. SHIMA, J. TANJI, Involvement of NMDA and Non-NMDA Receptors in the Neuronal Responses of the Primary Motor Cortex to Input from the Supplementary Motor Area and Somatosensory Cortex: Studies of Task-Performing Monkeys. *Jpn J Physiology*. 48, 275–290 (1998).

59. R. Meller, S. J. Thompson, T. A. Lusardi, A. N. Ordonez, M. D. Ashley, V. Jessick, W. Wang, D. J. Torrey, D. C. Henshall, P. R. Gafken, J. A. Saugstad, Z.-G. Xiong, R. P. Simon, Ubiquitin Proteasome-Mediated Synaptic Reorganization: A Novel Mechanism Underlying Rapid Ischemic Tolerance. *J Neurosci*. 28, 50–59 (2008).

60. M. J. Hasbani, M. L. Schlief, D. A. Fisher, M. P. Goldberg, Dendritic Spines Lost during Glutamate Receptor Activation Reemerge at Original Sites of Synaptic Contact. *J Neurosci*. 21, 2393–2403 (2001).

61. H. J. Kim, J. J. Waataja, S. A. Thayer, Cannabinoids Inhibit Network-Driven Synapse Loss between Hippocampal Neurons in Culture. *J Pharmacol Exp Ther*. 325, 850–858 (2008).

62. S. Graber, S. Maiti, S. Halpain, Cathepsin B-like proteolysis and MARCKS degradation in sub-lethal NMDA-induced collapse of dendritic spines. *Neuropharmacology*. 47, 706–713 (2004).

63. J. Cousineau, V. Plateau, J. Baufreton, M. L. Bon-Jégo, Dopaminergic modulation of primary motor cortex: From cellular and synaptic mechanisms underlying motor learning to cognitive symptoms in Parkinson's disease. *Neurobiol Dis*. 167, 105674 (2022).

64. J. A. Hosp, H. E. Nolan, A. R. Luft, Topography and collateralization of dopaminergic projections to primary motor cortex in rats. *Exp Brain Res*. 233, 1365–1375 (2015).

65. M. J. West, Stereological methods for estimating the total number of neurons and synapses: issues of precision and bias. *Trends Neurosci*. 22, 51–61 (1999).